



# Raman spectroscopy study of C-O-H-N speciation in reduced basaltic glasses: Implications for reduced planetary mantles

Celia Dalou<sup>a,b,\*</sup>, Marc M. Hirschmann<sup>b</sup>, Steven D. Jacobsen<sup>c</sup>, Charles Le Losq<sup>d</sup>

<sup>a</sup> Centre de Recherches Pétrographiques et Géochimiques, 15 rue Notre-Dame des Pauvres, BP20, 54501 Vandoeuvre-lès-Nancy Cedex, France

<sup>b</sup> Dept. of Earth Sciences, 108 Pillsbury Hall, University of Minnesota, Minneapolis, MN 55455, USA

<sup>c</sup> Department of Earth and Planetary Sciences, Northwestern University, Evanston, IL 60208, USA

<sup>d</sup> Research School of Earth Sciences, The Australian National University, Building 142, Mills Road, Canberra, ACT 2601, Australia

Received 11 January 2019; accepted in revised form 23 August 2019; available online 3 September 2019

## Abstract

To better understand the solution of volatile species in a reduced magma ocean, we identify via Raman spectroscopy the nature of C-O-H-N volatile species dissolved in a series of reduced basaltic glasses. The oxygen fugacity ( $f_{O_2}$ ) during synthesis varied from highly reduced at two log units below the iron-wüstite buffer (IW-2.1) to moderately reduced (IW-0.4), spanning much of the magmatic  $f_{O_2}$  conditions during late stages of terrestrial accretion. Raman vibrational modes for  $H_2$ ,  $NH_2$ ,  $NH_3$ ,  $CH_4$ ,  $CO$ ,  $CN^-$ ,  $N_2$ , and  $OH^-$  species are inferred from band assignments in all reduced glasses. The integrated area of Raman bands assigned to  $N_2$ ,  $CH_4$ ,  $NH_3$  and  $H_2$  vibrations in glasses increases with increasing molar volume of the melt, whereas that of  $CO$  decreases. Additionally, with increasing  $f_{O_2}$ ,  $CO$  band areas increase while those of  $N_2$  decrease, suggesting that the solubility of these neutral molecules is not solely determined by the melt molar volume under reduced conditions. Coexisting with these neutral molecules, other species as  $CN^-$ ,  $NH_2^-$  and  $OH^-$  are chemically bonded within the silicate network. The observations indicate that, under reduced conditions, (1)  $H_2$ ,  $NH_2$ ,  $NH_3$ ,  $CH_4$ ,  $CO$ ,  $CN^-$ ,  $N_2$ , and  $OH^-$  species coexist in silicate glasses representative of silicate liquids in a magma ocean (2) their relative abundances dissolved in a magma ocean depend on melt composition,  $f_{O_2}$  and the availability of H and, (3) metal-silicate partitioning or degassing reactions of those magmatic volatile species must involve changes in melt and vapor speciation, which in turn may influence isotopic fractionation.

© 2019 Elsevier Ltd. All rights reserved.

**Keywords:** Magma ocean; Volatiles; Oxygen fugacity; Nitrogen; Carbon; Hydrogen; Raman spectroscopy

## 1. INTRODUCTION

Magma oceans are expected during the late stages of Earth's accretion (e.g., [Elkins-Tanton, 2012](#)) and these large-scale melting events are likely to have produced mul-

tle episodes of volatile degassing to a primitive Hadean atmosphere ([Zahnle et al., 2007](#); [Hirschmann, 2012](#); [Tucker and Mukhopadhyay, 2014](#)). The character of this very early atmosphere remains poorly constrained, but was influenced in part by the redox state of the shallow portion of the magma oceans as they degassed ([Hirschmann, 2012](#)). Redox conditions in magma oceans are likely to have evolved together with melting depth and the compositions of accreting bodies ([Rubie et al., 2011](#)). Recent models have argued for conditions ranging between  $-4$  log units from

\* Corresponding author at: Centre de Recherches Pétrographiques et Géochimiques, 15 rue Notre-Dame des Pauvres, BP20, 54501 Vandoeuvre-lès-Nancy Cedex, France.

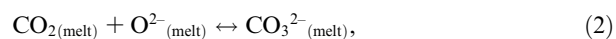
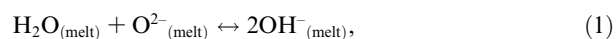
E-mail address: [cdalou@crpg.cnrs-nancy.fr](mailto:cdalou@crpg.cnrs-nancy.fr) (C. Dalou).

the iron-wüstite (IW) oxybarometer ( $\sim$ IW-4; Rubie et al., 2011) to  $\sim$ IW-1 (Siebert et al., 2013), but these apply to conditions at the locus of equilibration between silicate melt and core-destined metal. Degassing occurred shallower in the magma column, where redox conditions may have been different (Hirschmann, 2012; Zhang et al., 2017) and this may have had important control on the nature of dissolved C-O-H-N species, which in turn influenced the outgassing of the nascent Hadean atmosphere.

The dissolution of C-O-H-N in melts under reducing conditions is known to be complex, involving combinations of H, O-H, C-O, and C-H species (Mysen and Fogel, 2010; Hirschmann, 2012; Ardia et al., 2013; Dasgupta et al., 2013; Armstrong et al., 2015; Kadik et al., 2013, 2015, 2017) (Table S-1). Speciation of N seems to be particularly intricate, involving multiple N-H species, N<sub>2</sub> molecules, and nitride ions (Libourel et al., 2003; Mysen and Fogel, 2010; Kadik et al., 2013, 2015, 2017; Mosenfelder et al., 2019) (Supplementary information, Table S-1).

In this study we present a series of C-O-H-N -bearing basaltic glasses quenched from high pressure and temperature (1–3 GPa and 1400–1600 °C) synthesized over a range of reduced conditions (IW-2.1 to IW –0.4) representative of the late stages of magma oceans. Though magma oceans should be ultramafic, challenges in quenching such low viscosity liquids lead us to use basaltic compositions as approximate analogs. In the range of  $f_{O_2}$  studied (IW-0.4 to IW-2.1 Table 1), the “total H” content and C content increase, whereas N content decreases with increasing  $f_{O_2}$  (Fig. 1). However, these C-O-H-N -bearing basaltic glasses are not vapor saturated; instead their H, C and N contents are controlled by equilibrium exchange with a metal alloy (Dalou et al., 2017). Moreover, analytical determinations of H, C and N concentrations do not reveal the underlying distribution of C-O-H-N species (for instance, OH<sup>-</sup>, H<sub>2</sub>, CH<sub>4</sub> and NH<sub>3</sub> likely contribute to “total H”). Therefore to better understand controls on H, C and N speciation in reduced basaltic glasses, we present Raman spectroscopic observations, which place new constraints on the magmatic speciation of C-O-H-N species under reduced conditions. Note that for the different individual species detected in the reduced glasses, Raman cross-sections are expected to vary. Thus, the band areas observed give relative (albeit qualitative) species abundances.

The speciation of volatiles in amorphous silicate changes with temperature and during quench (e.g., Nowak and Behrens 1995; Nowak et al. 2003). For instance, temperature-dependent speciation changes are known for dissolved H<sub>2</sub>O and CO<sub>2</sub>, whereby the reactions



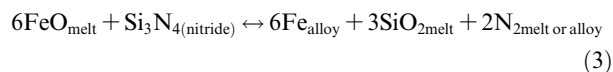
shift to the left with decreasing temperature. Nevertheless, speciation is frozen-in below the glass transition temperatures (e.g., Sowerby and Keppler 1999). To our knowledge, such effects on N-O-H species has not been determined, but temperature effects are probable. Although we cannot ascertain the magnitude of such effects on the glasses stud-

ied in this work, (1) results from Mysen and Fogel (2010) show that N speciation differences in the melts at *HT* and at their glass transition temperature are small; and (2) C-O-H-N species silicate melts observed by Raman spectroscopy *in situ* during hydrothermal diamond anvil cell experiments (e.g., Mysen, 2015, 2016, 2018) are in qualitative agreement with the speciation of H, C and N presented below. However, these HDAC experiments do not permit observation of speciation below the IW buffer or for silicate melt compositions representative of planetary magma oceans (Mysen, 2015, 2016, 2018). Here we explore the interaction between different C-O-H-N individual species in reduced basaltic glasses using variations in Raman band areas, and examine the influence of *P*, *T*, and  $f_{O_2}$ , H<sub>2</sub> relative proportion, and glasses’ molar volume on the speciation of H, C and N.

## 2. METHODS

### 2.1. Experimental methods

The glasses in this study were synthesized and characterized by electron probe microanalysis (EPMA) and secondary ion mass spectrometry (SIMS) by Dalou et al. (2017). Starting synthetic basaltic compositions include one based on the Adirondack-class Humphrey basalt (noted HB) from Gusev Crater, Mars, close in composition to that used by Stanley et al. (2014) and Armstrong et al. (2015) and another similar to the normal MORB composition (noted MORB) used by Armstrong et al. (2015). Following mixing of base basalt powder compositions, variable amounts of Fe<sub>4</sub>N and Si<sub>3</sub>N<sub>4</sub> were added as N sources; the graphite capsules from high-pressure experiment provided the source of C. Oxygen fugacity ( $f_{O_2}$ ) was varied (but not controlled) by varying the amount of Si<sub>3</sub>N<sub>4</sub> added to starting compositions, based on the reaction:



The high-pressure experiments were designed to equilibrate graphite saturated basaltic glasses with Fe-C-N alloys over a range of redox conditions (IW-0.4 to IW-2.1, Table 1). No water was deliberately introduced and  $f_{H_2O}$  was not fixed, but measured “H” in the samples (Table 1) results from contamination of the starting materials and from H<sub>2</sub>O introduced during piston cylinder experiments (e.g., Médard et al., 2008). Although H, C, and N concentrations in the melt varied depending on the experimental  $f_{O_2}$  (Table 1), in no cases were they saturated, as no vapor bubbles are apparent in the quenched samples.

Experiments were performed in a piston cylinder apparatus at 1.2, 2, or 3 GPa and 1400 or 1600 °C (Table S-1). Up to 6 compositions were loaded simultaneously into individual 0.8- to 1.2-mm-diameter holes drilled into a single graphite rod. Following analysis by EPMA and SIMS, reported in Dalou et al. (2017), the gold coating was removed and samples were cleaned and dried for analysis by Raman spectroscopy.

Table 1

Experimental conditions, molar volume (Vm) and low-wavenumber (WN) band frequency ( $\text{cm}^{-1}$ ), full-width-at-half maximum (FWHM, in  $\text{cm}^{-1}$ ), and normalized area (NA) along with associated errors.

Sample	P (GPa)	T (°C)	$\log f_{\text{O}_2}$	$\Delta\text{IW}$	$\text{H}_2\text{O}$ (wt.%) <sup>*</sup>	C (ppm) <sup>*</sup>	N (wt.%) <sup>*</sup>	Vm	CO bands			CN bands			N <sub>2</sub> bands					
									WN	FWHM	NA	WN	FWHM	NA	WN	FWHM	NA	WN	FWHM	NA
<b>B706A</b>	1.2	1400	−10.2	−1.2	0.68(1)	78(1)	0.09(1)	21.3	2123	50	0.63(2)	2268	39	0.07(1)	2332	11	0.24(1)	2340	16	0.06(2)
<b>B706B</b>	1.2	1400	−10.3	−1.3	0.500(4)	70(1)	0.09(1)	21.4	2122	58	0.62(3)	2263	35	0.08(1)	2331	10	0.21(2)	2338	16	0.09(1)
<b>B706C</b>	1.2	1400	−9.8	−0.7	1.043(5)	110(1)	0.04(1)	20.6	2119	59	0.72(8)	2267	30	0.06(2)	2331	10	0.18(3)	2340	16	0.04(3)
<b>B707B</b>	2	1400	−9.3	−0.4	1.29(10)	141(11)	0.13(2)	19.8	2122	58	0.57(5)	2267	33	0.05(2)	2331	8	0.17(2)	2336	20	0.22(2)
<b>B707C</b>	2	1400	−9.7	−0.9	0.86(2)	101(1)	0.23(1)	20.7	2126	61	0.48(3)	2263	38	0.05(1)	2331	9	0.22(4)	2337	18	0.26(4)
<b>B712A</b>	2	1600	−7.9	−0.7	0.716(1)	487(1)	0.14(1)	19.9	2113	56	0.91(2)	2268	35	0.02(1)	2331	9	0.03(1)	2336	20	0.04(1)
<b>B712C</b>	2	1600	−8.2	−1.1	na	na	0.12(2)	20.3	2117	52	0.91(1)	2267	39	0.010(3)	2333	9	0.04(8)	2338	20	0.05(1)
<b>B712D</b>	2	1600	−9.1	−2.1	0.289(4)	195(2)	0.78(1)	21.3	2123	46	0.73(4)	2262	37	0.05(1)	2331	9	0.10(4)	2337	16	0.13(4)
<b>B712E</b>	2	1600	−8.4	−1.2	0.49(2)	258(5)	0.26(1)	20.8	2121	49	0.82(1)	2262	40	0.03(1)	2332	8	0.06(1)	2336	18	0.10(1)
<b>B712F</b>	2	1600	−8.0	−0.8	0.721(5)	328(71)	0.14(2)	20.1	2116	58	0.89(2)	2268	39	0.02(1)	2332	10	0.05(2)	2337	18	0.04(2)
<b>B727A</b>	2	1600	−8.5	−1.3	0.415(3)	212(5)	0.34(2)	21.1	2117	52	0.84(1)	2263	36	0.025(4)	2332	8	0.050(4)	2337	20	0.09(1)
<b>B727B</b>	2	1600	−8.3	−1.1	0.75(1)	270(16)	0.21(2)	20.8	2118	51	0.87(2)	2268	36	0.017(5)	2332	9	0.04(1)	2336	20	0.07(1)
<b>B727C</b>	2	1600	−8.6	−1.4	0.604(3)	192(5)	0.16(3)	21.0						<i>below detection</i>						
<b>B727D</b>	2	1600	−9.0	−1.8	1.02(2)	213(83)	0.19(2)	20.4	2117	53	0.82(2)	2268	31	0.031(8)	2333	8	0.053(7)	2338	21	0.09(1)
<b>B727E</b>	2	1600	−9.0	−1.8	0.57(1)	270(13)	0.24(1)	21.1	2119	54	0.84(2)	2274	37	0.019(6)	2333	10	0.053(1)	2338	21	0.09(2)
<b>B727F</b>	2	1600	−8.5	−1.3	0.33(1)	222(17)	0.26(1)	21.0	2119	55	0.89(1)	2265	34	0.012(4)	2332	10	0.053(6)	2339	17	0.05(1)
<b>B714A</b>	3	1600	−7.9	−0.4	na	na	0.17(2)	18.7	2112	58	0.89(2)	2262	34	0.012(4)	2332	10	0.04(1)	2337	21	0.06(1)
<b>B714B</b>	3	1600	−8.5	−1.1	0.493(2)	239(7)	0.43(1)	19.4	2119	57	0.81(1)	2267	33	0.012(4)	2333	10	0.072(5)	2338	22	0.11(1)
<b>B714C</b>	3	1600	−9.1	−1.6	0.361(4)	166(9)	1.230(2)	19.8	2125	54	0.66(4)	2268	33	0.020(4)	2332	9	0.14(2)	2339	19	0.19(2)
<b>B714D</b>	3	1600	−8.5	−1.1	0.59(2)	223(32)	0.38(2)	19.3	2118	59	0.82(2)	2266	31	0.012(4)	2332	9	0.05(1)	2337	19	0.11(1)

Numbers in parentheses reflect  $2\sigma$  standard errors in the significant digit from best-fit results.

<sup>\*</sup> From Dalou et al. (2017). Numbers in parentheses for N, H content represent one standard deviation in the significant digit.

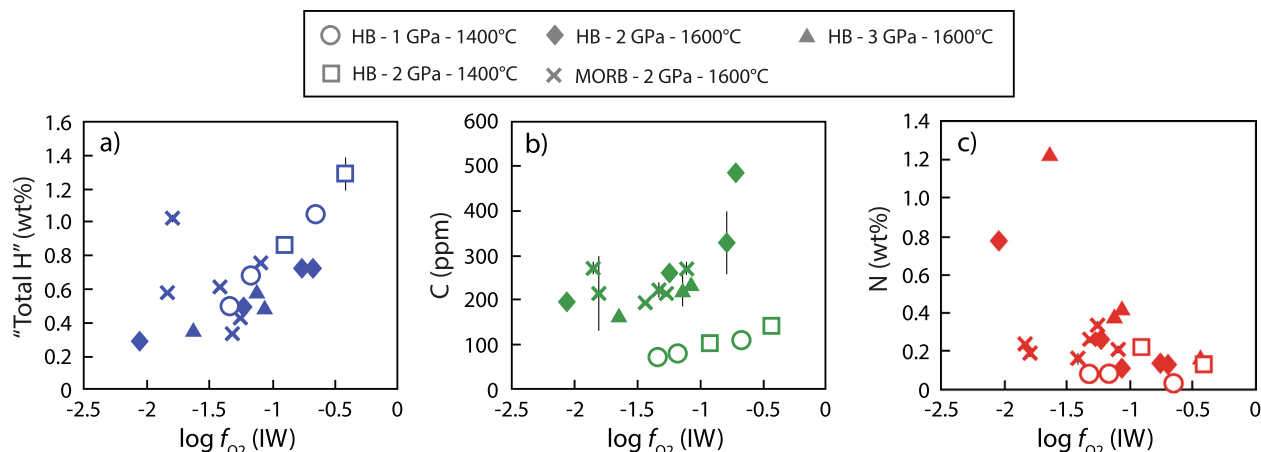


Fig. 1. Variation of (a) “total H” (refers to the sum of  $\text{OH}^-$ ,  $\text{H}_2$  and C-H and N-H species), (b) C and (c) N content with  $\log f_{\text{O}_2}$  relative to the IW buffer. Concentrations are from Dalou et al. (2017).

## 2.2. Analytical methods

Major element and N concentrations of silicate glasses determined by EPMA, as well as C and total H<sub>i</sub> (reported as “H<sub>2</sub>O”, but including  $\text{OH}^-$ ,  $\text{H}_2\text{O}$ ,  $\text{NH}_x$ ,  $\text{CH}_x$ , and  $\text{H}_2$  species) determined by SIMS (Table 1), are documented in Dalou et al. (2017).

Raman spectroscopy was conducted using a custom-built, confocal micro-Raman system that includes a 458 nm solid-state diode laser source (Melles Griot 85-BLS-601) with 300 mW output. The laser intensity was reduced with neutral density filters to 10 mW power at the sample through a 100x Mitutoyo M Plan Apo objective lens with 6 mm working distance and 0.7 numerical aperture. The use of the 100x objective allowed a spatial resolution of 1–2  $\mu\text{m}$ . Compared to a more conventional green-laser excitation system, use of a 458 nm (blue) excitation source not only improves the intensity of the Raman scattering, but also positions molecular vibrations from volatile species in the 2000–4000  $\text{cm}^{-1}$  region in the mid-part of the visible region, where the Andor Newton DU970 CCD camera used to collect the spectra has  $\sim 95\%$  quantum efficiency. Scattered light was collected through a confocal aperture into a 0.3 m focal length Andor Shamrock spectrometer with 1200 lines per mm holographic grating, with the spectral window centered at 1250  $\text{cm}^{-1}$  and 3400  $\text{cm}^{-1}$  for low and high wavenumber measurements, respectively. The spectral resolution ranges from 1.2 to 1.8  $\text{cm}^{-1}$  at 100–3500  $\text{cm}^{-1}$  Raman shift. Spectra were obtained for 30 seconds, averaged over 10 accumulations. With these acquisition settings and reduced power of 10 mW, Raman spectra in the O-H region of a vitreous silica ( $v\text{-SiO}_2$ ) glass standard (KOG, Thomas et al., 2015) containing 332 ( $\pm 20$ ) ppm  $\text{H}_2\text{O}$  by weight exhibits a signal-to-noise ratio of about 20:1.

The experiments of Dalou et al. (2017) produced glasses more reduced than IW-2.1, but Raman examination produced too much fluorescence to accurately perform background corrections (Fig. S-1). The reason for this fluorescence is not known, but is presumably owing to

stabilization of a fluorescent transition metal ion at highly reduced conditions (Baert et al., 2011).

## 2.3. Peak fitting procedure

Baseline correction and deconvolution of Raman spectra were performed using the IGOR software package from Wavemetrics Inc. Low and high wavenumber spectra, from 1950 to 2230  $\text{cm}^{-1}$  and from 2380 to 4230  $\text{cm}^{-1}$  respectively, were processed separately. A linear baseline was used for the low wavenumber part of the Raman signal, while a spline correction was fitted for the high wavenumber baseline (Fig. 2). For the fitting procedure, Raman shift, peak width, and intensity were treated as independent variables with convergence criterion based on the minimization of  $\chi^2$ .

In the 1950–2550  $\text{cm}^{-1}$  range (Fig. 3), three bands are observed at 2110, 2265, and 2330  $\text{cm}^{-1}$ . The 2330  $\text{cm}^{-1}$  band shows an asymmetry that could not be accounted for by using Gaussian, Voigt, nor Lorentzian functions. Instead, this feature was deconvolved into two Gaussian peaks: one at 2332  $\text{cm}^{-1}$  and one at  $\sim 2338$   $\text{cm}^{-1}$  (Fig. 3). The 2332  $\text{cm}^{-1}$  peak is very narrow with a FWHM (Full Width at Half Maximum) between 8 and 11  $\text{cm}^{-1}$  (Table 1). The bands at 2110 and 2265  $\text{cm}^{-1}$  were fitted with Gaussian peaks. To fit these bands, the position and width of the 2332  $\text{cm}^{-1}$  peak was first fixed, and then all the variables (shift, FWHM, and band intensity) were optimized without constraint.

In the 2800–4400  $\text{cm}^{-1}$  region of the Raman spectra (Fig. 2), multiple peaks are observed. In the interval between 2850–2900  $\text{cm}^{-1}$ , two peaks can be fitted, in agreement with Mysen (2015). The broad asymmetric peak with maximum intensity around 3550  $\text{cm}^{-1}$  is well-approximated by two Gaussian bands, with one centered at  $\sim 3500$   $\text{cm}^{-1}$  and the other at  $\sim 3580$   $\text{cm}^{-1}$ , following Foustoukos and Mysen (2012). Mysen and Fogel (2010) fit the three sharp peaks spanning 3100 to 3400  $\text{cm}^{-1}$  with three bands. In contrast, Kadik et al. (2015) employed four bands to match Raman shifts observed in the same interval. Obtaining a fit for this portion of the spectra that matched observations to

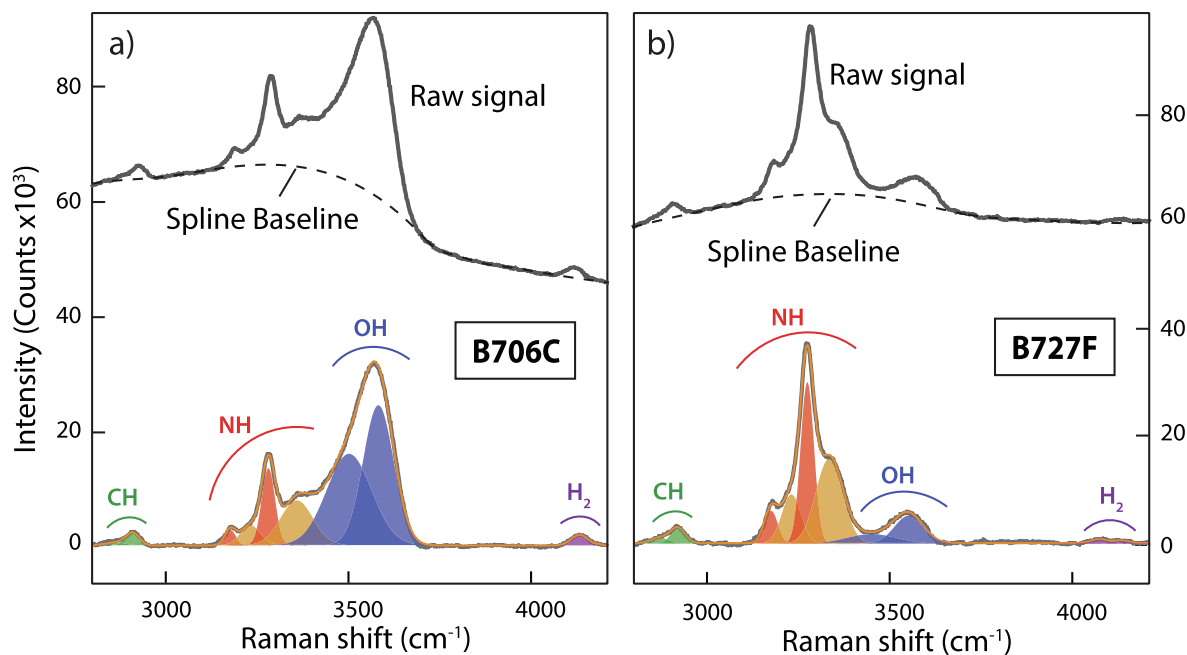


Fig. 2. Examples of spline baseline corrections (dashed curve) and peak fitting in the 2800 to 4400  $\text{cm}^{-1}$  portion of two Raman spectra from glasses (a) B706C (0.09 wt.%, 0.50 wt.% “total H” and IW-1.3) and (b) B727F (0.26 wt.%, 0.33 wt.% “total H” and IW-1.3). The grey curves correspond to the Raman spectra and the orange curves are the peak fits. (See text for discussion of band assignments).

within 5–10% required four peaks near 3180, 3250, 3280, and 3350  $\text{cm}^{-1}$  (while fitting three bands in this portion produced an intensity difference between the spectra and the fit higher than 20%). Finally, a peak around 4130  $\text{cm}^{-1}$  is also fitted with two Gaussian peaks: one at 4130  $\text{cm}^{-1}$  and a second at 4200  $\text{cm}^{-1}$ . In some of the spectra this high wavenumber feature appears simply as single asymmetric band, and in others, two clearly distinguishable peaks are evident. The centroid and width of these two peaks were guided by those spectra for which the clearly distinguishable peaks could be present.

In total, ten peaks were fitted from the observed spectra. Preliminary fits of individual bands were carried out with Raman shift and FWHM as fixed variables based on previous work from Mysen (2015) for the 2800–2900  $\text{cm}^{-1}$  portion, from Kadik et al. (2015) for the 3100 to 3400  $\text{cm}^{-1}$  region and from Foustoukos and Mysen (2012) for the 3450–3700  $\text{cm}^{-1}$  region. In successive refinements, the preliminary fit was used with FWHM left unconstrained and in the final step, all variables were unconstrained. The fits were judged satisfactory when the intensity difference between the spectra and the fits was less 5% for spectra with low noise, i.e. a signal-to-noise ratio of about 2.5:1 on weak bands around 2870 and 4130  $\text{cm}^{-1}$ . For spectra corresponding to  $f_{\text{O}_2}$  between IW-1.8 and IW-2.1 with a lower signal-to-noise ratio, the best fits were achieved with a fit to spectra difference between 5 and 10%.

### 3. RESULTS

#### 3.1. Raman Peak assignment

The peaks at 2110 and 2230  $\text{cm}^{-1}$  are assigned to triple bonded  $\text{C}\equiv\text{O}$  stretching (Wetzel et al., 2013; Yoshioka

et al., 2015), and triple bonded  $\text{N}_2$  stretching (Lofthus and Krupenie, 1977), respectively. Although the 2330  $\text{cm}^{-1}$  ( $\text{N}_2$  stretching) peak is commonly attributed to atmospheric  $\text{N}_2$  (Klimm and Botcharkin, 2010; Li et al. 2015a, 2017), in the glasses in this study the feature arises in part from dissolved nitrogen (Fig. 3), as also noted by Roskosz et al. (2006) and Kadik et al. (2013). A weak, although not insignificant, peak appears between 2260 and 2275  $\text{cm}^{-1}$  (Fig. 3). This peak cannot be attributed to a nitrosyl group ( $-\text{NO}$ ) vibration, which is found in the range 2050–2100  $\text{cm}^{-1}$  in silicate glasses (Roskosz et al. 2006). Instead, it could correspond to triple bonded  $\text{C}\equiv\text{N}$  stretching (Socrates, 2001). Indeed,  $\nu(\text{C}\equiv\text{N})$  band is detected at 2258  $\text{cm}^{-1}$  in cyanamide, at 2261  $\text{cm}^{-1}$  in malonitrile and at 2274  $\text{cm}^{-1}$  in cyanoacetamide (Parker and Hope, 2010, and references therein).

The two peaks at 2860 and 2900  $\text{cm}^{-1}$  (Fig. 4a and b) are assigned to C-H stretching in agreement with  $^{13}\text{C}$  magic angle spinning nuclear magnetic resonance data on C-O-H-bearing aluminosilicate glasses (Mysen et al., 2011). The peak at 2900  $\text{cm}^{-1}$  is assigned to C-H stretching in  $\text{CH}_4$  (e.g., Ardia et al., 2013; Mysen, 2015). The assignment of the peak around 2870  $\text{cm}^{-1}$  is often assigned to C-H stretching vibration in  $\text{Si-CH}_3$  (Mysen and Yamashita, 2010; Mysen, 2015).

The broad asymmetric peak with maximum intensity around 3550  $\text{cm}^{-1}$  is assigned to  $\text{OH}^-$  stretching vibrations. As observed in hydrous glasses, this peak extends between 2800 and 4000  $\text{cm}^{-1}$  (e.g., McMillan and Remmele, 1986; Frantz et al., 1993), forming the background below the peaks assigned to N-H and C-H stretching (Fig. 2). Its asymmetry results from the complex bonding of water in silicate glasses (e.g., Le Losq et al., 2015). The Gaussian band centered near 3580  $\text{cm}^{-1}$  is assigned to isolated  $\text{OH}^-$

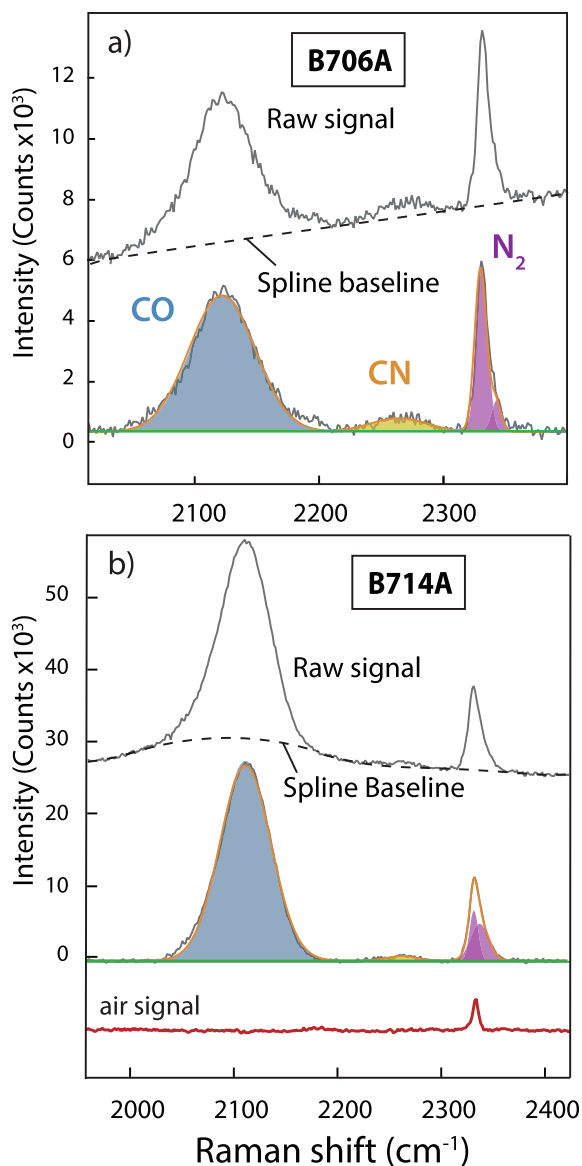


Fig. 3. Examples of spline baseline corrections (dashed curve) and of peak fitting in the 1950 to 2550  $\text{cm}^{-1}$  portion of the Raman spectra of glasses B706A and B714A. The red spectrum (at the bottom of panel b) is from a pure amorphous silica standard with known  $\text{H}_2\text{O}$  content (KOG from Thomas et al. 2015). As for Fig. 2, the grey curve corresponds to the Raman spectra and the orange curve is the peak fit. (See text for discussion of band assignments).

groups and the other near 3500  $\text{cm}^{-1}$  is assigned to isolated and hydrogen-bonded  $\text{OH}^-$  groups (Foustoukos and Mysen, 2012).

The four peaks near 3180, 3250, 3280, and 3350  $\text{cm}^{-1}$  are assigned to N-H stretching (Roskosz et al., 2006; Mysen et al., 2008; Kadik et al., 2017). Lautié et al. (1976) suggest that NH stretching frequency is primarily controlled by hydrogen bond strength. However, work on water-bearing silicate melts showed that the extent of hydrogen bonding in hydrous silicate melts is controlled by temperature and melt structure (e.g., Le Losq et al., 2015, 2017), such that those parameters ultimately deter-

mine O-H band position. For N-H bonding, the four different bands related to N-H stretching likely correspond to different NH chemical groups (e.g.,  $\text{NH}_2^-$  and/or  $\text{NH}_3$ ). Nevertheless, based on both Raman and FTIR studies, the assignment of these bands to  $\text{NH}_2^-$  and/or  $\text{NH}_3$  is not straightforward and still debated (Mysen et al., 2008; Mysen and Fogel, 2010; Kadik et al., 2015, 2017; Mosenfelder et al., 2019). Mosenfelder et al. (2019) suggest that the bands near 3225 and 3370  $\text{cm}^{-1}$  are  $\text{NH}_2^-$  stretching vibrations, the one at 3285  $\text{cm}^{-1}$  is an  $\text{NH}_2^-$  stretching vibration and that the one near 3180  $\text{cm}^{-1}$  is an overtone of the bending mode of  $\text{NH}_2^-$ . In contrast, Mysen et al. (2008) and Mysen and Fogel (2010) assigned the 3310–3320  $\text{cm}^{-1}$  band to isolated  $\text{NH}_3$  molecules. Some of the reasoning from Mosenfelder et al. (2019) is based on FTIR features in the 1400–1600  $\text{cm}^{-1}$  region, but the Raman spectra in this region do not provide similar confirmatory observations, in part because these bands are weak in Raman spectra and also because in the present case, the 1400–1600  $\text{cm}^{-1}$  region has interferences from graphite and diamond vibrations (Fig. S-2), which are likely produced by graphite microinclusions (observed under reflective light, with a 100x objective) and diamond polishing powder, respectively.

The high intensity of N-H stretching bands and the large number of Raman spectra available in this study allow observations of inter-correlations between band intensities. Among the four peaks related to N-H stretching vibrations, we observe positive correlations between the 3180 and 3285  $\text{cm}^{-1}$  bands and between the 3235 and 3355  $\text{cm}^{-1}$  bands (Fig. 5), suggesting that these two sets of bands may each correspond to the same N-H molecules. For each correlated pair, the highest wavenumber bands (3285 and 3355  $\text{cm}^{-1}$ ) should correspond to asymmetric stretching vibrations, while the second bands (3180 and 3235  $\text{cm}^{-1}$ ) correspond to symmetric stretching (e.g., Lin-Vien et al., 1991, pp. 160–173). In zincate diamide (Richter et al., 2015) and in sulfanilamide compounds (Muthuselvi et al., 2017), a band at 3248–3250  $\text{cm}^{-1}$  with a strong Raman intensity but very weak in FTIR is assigned to an  $\text{NH}_2^-$  symmetric stretching vibration. Its corresponding asymmetric vibration is detected at 3355  $\text{cm}^{-1}$  by Muthuselvi et al. (2017). This assignment to  $\text{NH}_2^-$  is consistent with Mosenfelder et al. (2019).

In contrast, the origin of the bands at 3285 and 3180  $\text{cm}^{-1}$  is less certain. The correlation in the intensities of these bands (Fig. 4a) may not support their assignment to distinct species (e.g., 3285  $\text{cm}^{-1}$  to  $\text{NH}_2^-$  stretching vibration and 3180  $\text{cm}^{-1}$  to an overtone of the bending mode of  $\text{NH}_2^-$ ; Mosenfelder et al. 2019), though the correlation alone also does not exclude these assignments. An additional consideration is that the bands at 3180 and 3285  $\text{cm}^{-1}$  are narrower than those at 3235 and 3355  $\text{cm}^{-1}$  (Table 2), which, following the logic of Mysen et al. (2008) could suggest that bands at 3180 and 3285  $\text{cm}^{-1}$  correspond to uncharged free  $\text{NH}_3$  molecule (see also Nakamoto 2009, p. 159, 220). However, Mosenfelder et al. (2019) did not observe in FTIR the degenerate deformational mode at 1627  $\text{cm}^{-1}$  that would be expected for isolated  $\text{NH}_3$  molecules. Nevertheless, this

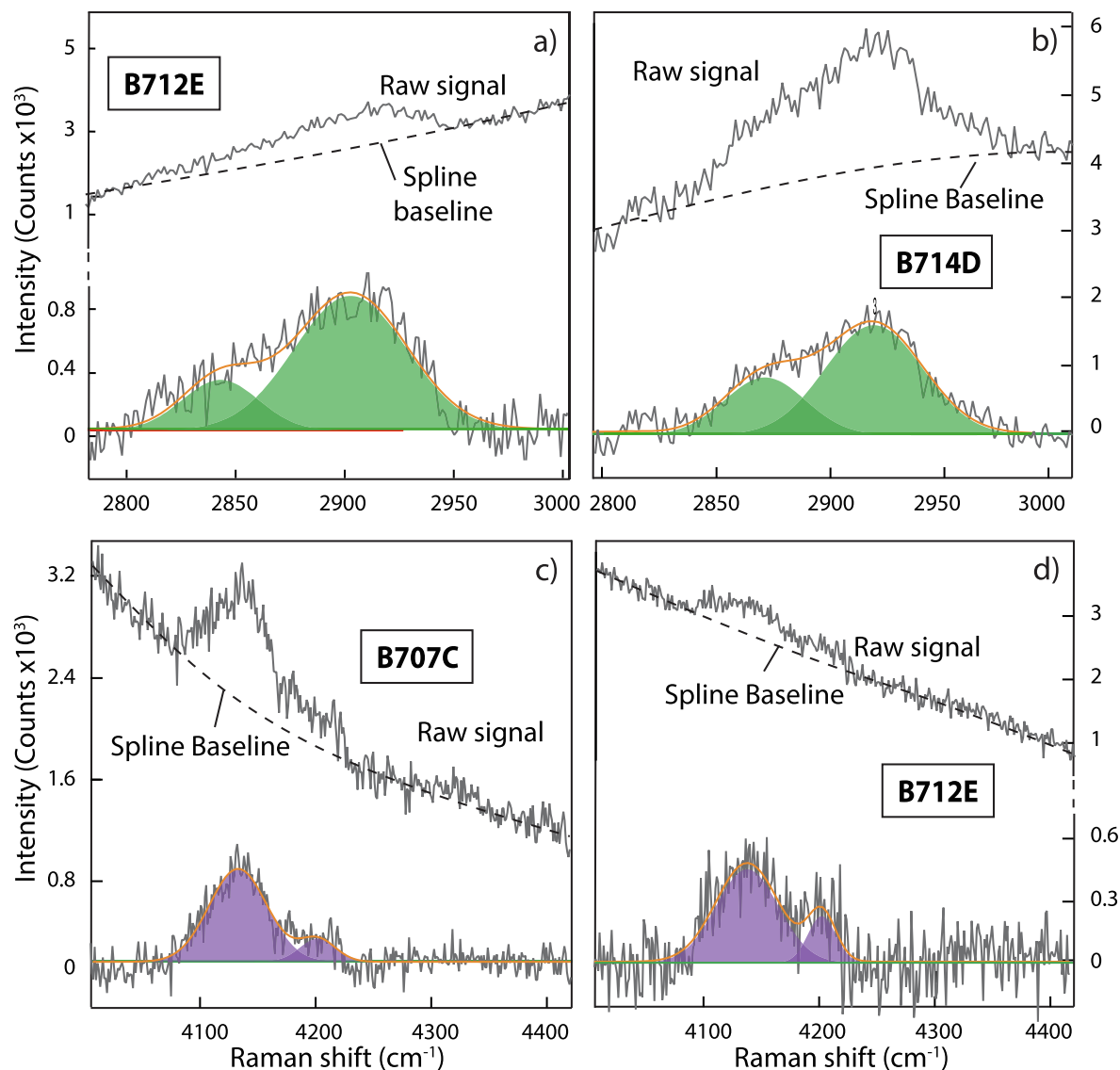


Fig. 4. Examples of spline baseline corrections (dashed curves) and peak fitting in the (a) 2800–3000  $\text{cm}^{-1}$  portion of the Raman spectra of glasses B712E and glass B714D, assigned to CH stretching vibration, and (b) 4050–4300  $\text{cm}^{-1}$  portion of the spectrum of glasses B707C and glass B712E, showing a visible band assigned to H-H stretching in  $\text{H}_2$ . The grey curves correspond to the Raman spectra and the orange ones to their fits. In both portion of the spectra, two Gaussian bands are necessary to fit this portion of the signal adequately. (For interpretation of the references to colour in this figure legend, the reader is referred to the web version of this article.)

NH bending mode of ammonia expected in the 1627  $\text{cm}^{-1}$  region is not always observed in  $\text{NH}_3$ -bearing silica glasses (Cant and Little, 1964). Further investigations are therefore necessary to assign the 3180 and 3285  $\text{cm}^{-1}$  bands.

Consistent with the conclusions of Mysen et al. (2008) and Mosenfelder et al. (2019), there are no features detected in the Raman spectra of our glasses that correspond to  $\text{NH}_4^+$  vibrations. These would include symmetric stretching vibration near 3470 and 3630  $\text{cm}^{-1}$  and overtones at 2880, 3030, and 3115  $\text{cm}^{-1}$  found in  $\text{NH}_4^+$ -bearing phases (Dong et al., 2007; Watenphul et al., 2009, and references therein).

The band near 4130  $\text{cm}^{-1}$  is assigned to dissolved molecular  $\text{H}_2$  (Hirschmann et al., 2012). The asymmetry of the  $\text{H}_2$  band (Fig. 4c and d) could reflect substitutions in multiple

local environments in the silicate network, as previously suggested by Schmidt et al. (1998). This reasoning may also apply to the observed asymmetry of the  $\text{N}_2$  band, mentioned above.

## 4. DISCUSSION

### 4.1. C-O-H-N dissolution in reduced basaltic glasses

In the reduced glasses from this study, carbon was detected as C-H complexes, CO and CN (Figs. 2, 3, 4a and b). The vibration mode of carbonate ion  $\text{CO}_3^{2-}$ , at 1085  $\text{cm}^{-1}$  (e.g., Bourgue and Richet, 2001), overlaps with Si-O stretching mode and therefore could not be detected.

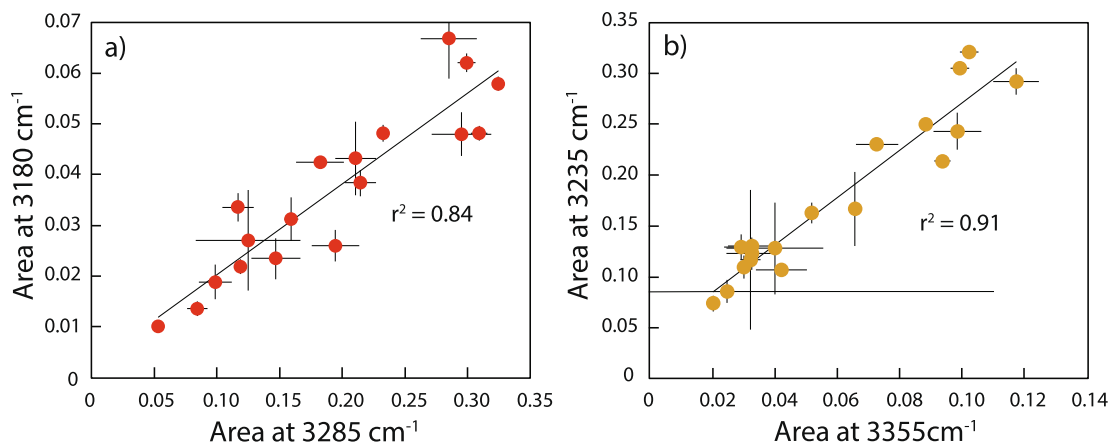
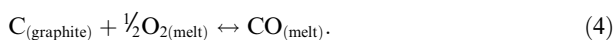


Fig. 5. Co-variation of Gaussian normalized band areas (a) 3180  $\text{cm}^{-1}$  versus 3285  $\text{cm}^{-1}$  and (b) 3235  $\text{cm}^{-1}$  versus 3355  $\text{cm}^{-1}$ . Error bars are  $2\sigma$ . The strong correlations between normalized band areas suggests that the bands belong to the same N-H molecules. Those bands are assigned to (a) to  $\text{NH}_3$  and (b) to  $\text{NH}_2$ . (See text for discussion of band assignments).

However, carbonate is expected only in very small quantities at the reduced conditions at which these glasses were synthesized (Stanley et al., 2014; Armstrong et al., 2015). For these reduced conditions, CO is the main carbon species in anhydrous glasses and potentially also in hydrous glasses (e.g., Wetzel et al., 2013; Armstrong et al., 2015; Yoshioka et al., 2015). CO bonds in reduced silicate glasses were not detected in many previous Raman studies, including those of Mysen et al. (2009, 2011) and Mysen (2013, 2015) who studied sodium silicate and aluminosilicate glasses, or Dasgupta et al. (2013) and Chi et al. (2014), who examined basaltic glasses similar in composition (including  $\text{H}_2\text{O}$  content) and quenched from comparable pressure and  $f_{\text{O}_2}$ . The Raman (and infrared active) band at 2110–2120  $\text{cm}^{-1}$  observed by Wetzel et al. (2013) was misidentified as a CO ligand in carbonyl groups in reduced basaltic glasses, and was later shown to be molecular CO by Yoshioka et al. (2015), as adopted by Armstrong et al. (2015). Observation of CO in Wetzel et al. (2013), Armstrong et al. (2015), and this study may be enhanced by the use of a 458 nm (blue) excitation line as compared to the 514 nm laser used in the studies of Mysen et al. (2009, 2011), Mysen (2013, 2015), Dasgupta et al. (2013), and Chi et al. (2014). Because  $\text{C}\equiv\text{O}$  bonds are strongly polarized (electronegativity of C: 2.55 versus O: 3.44), and CO concentrations comparatively small (<120 ppm; Armstrong et al., 2015), their Raman signals are weak. As Raman scattering intensity is inversely proportional to the fourth power of the excitation laser wavelength (Long 1977), a 458 nm excitation line enhances the C-O bond scattering intensity as compared to a 514 nm laser. Because CO is not easily detected, studies of C dissolution in reduced glasses have underestimated its importance and instead tended to emphasize the roles of methyl ( $\text{CH}_3$ ) groups and molecular  $\text{CH}_4$  (e.g., Mysen et al., 2009, 2011; Mysen and Yamashita, 2010; Mysen, 2013, 2015; Ardia et al., 2013; Dasgupta et al., 2013). CO is likely dissolving as:



In dry reduced melts, the concentration of reduced non-carbonate C correlates with  $f_{\text{CO}}$  with a slope close to 1 (Armstrong et al., 2015). Fig. 6a and Fig. 6b show that the area of the 2120  $\text{cm}^{-1}$  Raman band correlates with  $\log f_{\text{CO}}$  (calculated as described in Armstrong et al., 2015) and  $\log f_{\text{O}_2}$ , respectively. This correlation supports the conclusion that CO detected in silicate glasses is not owing to pentacarbonyl  $\text{Fe}(\text{CO})_5$ , (e.g., Wetzel et al., 2013; Stanley et al., 2014), but rather to isolated  $\text{C}\equiv\text{O}$  species (Yoshioka et al., 2015; Armstrong et al. 2015). The ionic porosity was introduced by Dowty (1980) and Fortier and Giletti (1989) and is related to the concept of free volumes in glasses (e.g., Turnbull and Cohen, 1961), free volumes being defined by the difference between the total molar volume and the volume of occupied by the constituent ions. Although the ionic porosity (IP) is a useful proxy of available space that can be filled by neutral gas molecules, quite different values of IP can be calculated depending on the method used (e.g., Carroll and Stolper, 1993; Paonita, 2005; Marrocchi and Toplis, 2005; Iacono-Marziano et al., 2010). Therefore, we chose to use molar volume of the melt, expressed in  $\text{cm}^3/\text{mole}$ , which offers a more direct comparison among literature data, as its calculation depends simply on glass compositions,  $P$  and  $T$ . Like noble gas solubilities (as Ar, Ne and He; e.g., Carroll and Stolper, 1993; Paonita, 2005; Marrocchi and Toplis, 2005), CO peak area correlates with the molar volume of the melt (Fig. 6c). In this particular case, assuming that concentrations of neutral molecules show systematic variation with molar volume while those of bonded molecules do not (Fig. S-3), the correlations between CO peak area with the melt volume are consistent with the interpretation that it arises from  $\text{C}\equiv\text{O}$  stretching in a neutral molecule with a dipole moment that interacts weakly with the silicate matrix (Yoshioka et al., 2015). Contrary to that of other neutral molecules like  $\text{N}_2$ ,  $\text{CH}_4$ ,  $\text{NH}_3$  and  $\text{H}_2$  (see following discussion), the CO band area decreases with molar volume (Fig. 6c).

C-H vibrations have intense Raman signals, even at low concentrations (Ardia et al., 2013; Chi et al., 2014).



Table 2

Experimental conditions and high-wavenumber (WN) band frequency ( $\text{cm}^{-1}$ ), full-width-at-half maximum (FWHM, in  $\text{cm}^{-1}$ ), normalized area (NA) along with associated errors.

Sample	$P$ (GPa)	$T$ ( $^{\circ}\text{C}$ )	$\log f_{\text{O}_2}$	CH bands									OH bands						$\text{H}_2$ bands											
				WN			FWHM			NA			WN			FWHM			NA			WN			FWHM			NA		
				WN	FWHM	NA	WN	FWHM	NA	WN	FWHM	NA	WN	FWHM	NA	WN	FWHM	NA	WN	FWHM	NA	WN	FWHM	NA	WN	FWHM	NA			
<b>B706A</b>	1.2	1400	−10.2	2867	66	0.015(4)	2909	41	0.027(5)	3519	141	0.24(10)	3593	97	0.31(10)	4132	73	0.015(3)	4206	32	0.004(1)									
<b>B706B</b>	1.2	1400	−10.3	2866	53	0.016(2)	2909	38	0.025(3)	3516	161	0.32(1)	3591	96	0.31(1)	4125	58	0.015(1)	4195	54	0.004(1)									
<b>B706C</b>	1.2	1400	−9.8	2845	44	0.009(2)	2906	52	0.036(5)	3492	161	0.37(6)	3582	103	0.39(6)	4125	57	0.015(1)	4199	33	0.001(1)									
<b>B707B</b>	2	1400	−9.3	2863	56	0.004(1)	2911	44	0.010(2)	3503	104	0.33(7)	3583	98	0.35(7)	4134	53	0.011(2)	4186	15	0.0001(1)									
<b>B707C</b>	2	1400	−9.7	2866	64	0.013(2)	2914	38	0.009(1)	3522	135	0.15(7)	3592	94	0.26(7)	4128	71	0.011(2)	4204	76	0.006(1)									
<b>B712A</b>	2	1600	−7.9	2817	21	0.002(1)	2895	88	0.05(1)	3498	147	0.25(9)	3579	96	0.33(8)	4128	65	0.006(3)	4202	41	0.0001(1)									
<b>B712C</b>	2	1600	−8.2	2811	38	0.009(3)	2882	81	0.058(4)	3514	157	0.11(1)	3585	108	0.32(1)	4132	77	0.010(4)	4202	32	0.003(2)									
<b>B712D</b>	2	1600	−9.1									<i>strong fluorescence</i>																		
<b>B712E</b>	2	1600	−8.4	2842	51	0.011(2)	2903	58	0.028(3)	3526	103	0.075(4)	3589	86	0.128(4)	4141	63	0.015(2)	4203	20	0.002(1)									
<b>B712F</b>	2	1600	−8.0	2860	40	0.008(1)	2911	50	0.039(1)	3503	156	0.11(1)	3581	91	0.15(1)	4128	55	0.017(2)	4187	55	0.002(1)									
<b>B727A</b>	2	1600	−8.5	2862	53	0.010(1)	2913	45	0.034(2)	3543	142	0.22(1)	3594	83	0.118(5)	4129	60	0.008(1)	4165	41	0.00026(2)									
<b>B727B</b>	2	1600	−8.3	2862	53	0.010(1)	2914	45	0.034(2)	3523	124	0.2(1)	3588	87	0.2(1)	4133	57	0.008(2)	4196	33	0.002(1)									
<b>B727C</b>	2	1600	−8.6	2869	46	0.013(6)	2912	41	0.042(6)	3516	132	0.25(8)	3584	88	0.30(8)	4131	45	0.007(2)	4180	40	0.001(2)									
<b>B727D</b>	2	1600	−9.0	2865	47	0.011(2)	2913	44	0.027(7)	3551	101	0.12(4)	3591	84	0.11(4)	4133	81	0.006(6)	4207	53	0.007(3)									
<b>B727E</b>	2	1600	−9.0	2853	56	0.013(2)	2907	47	0.019(2)	3534	144	0.11(3)	3586	91	0.13(3)	4141	67	0.006(2)	4204	37	0.007(1)									
<b>B727F</b>	2	1600	−8.5	2862	60	0.013(8)	2913	50	0.028(8)	3464	106	0.011(1)	3600	88	0.174(2)	4131	55	0.011(3)	4194	51	0.005(3)									
<b>B714A</b>	3	1600	−7.9	2823	24	0.003(2)	2880	71	0.04(2)	3517	132	0.21(2)	3581	97	0.3(2)	4138	79	0.002(8)	4207	25	0.003(2)									
<b>B714B</b>	3	1600	−8.5	2850	58	0.009(1)	2913	60	0.021(1)	3496	150	0.078(3)	3585	98	0.106(2)	4121	79	0.009(1)	4184	53	0.002(1)									
<b>B714C</b>	3	1600	−9.1									<i>strong fluorescence</i>																		
<b>B714D</b>	3	1600	−8.5	2871	42	0.008(5)	2919	51	0.018(5)	3493	159	0.06(1)	3580	99	0.14(1)	4136	73	0.009(1)	4194	59	0.001(2)									
Sample	$P$ (GPa)	$T$ ( $^{\circ}\text{C}$ )	NH peaks																											
			WN	FWHM	NA	WN	FWHM	NA	WN	FWHM	NA	WN	FWHM	NA																
<b>B706A</b>	1.2	1400	3183	34	0.024(4)	3236	51	0.033(8)	3285	40	0.15(2)	3361	94	0.12(2)																
<b>B706B</b>	1.2	1400	3181	37	0.022(1)	3234	53	0.030(1)	3284	41	0.118(3)	3358	96	0.11(1)																
<b>B706C</b>	1.2	1400	3182	34	0.010(1)	3233	54	0.020(2)	3281	45	0.053(4)	3356	87	0.07(1)																
<b>B707B</b>	2	1400	3178	35	0.014(2)	3234	64	0.032(2)	3283	43	0.084(8)	3360	104	0.12(7)																
<b>B707C</b>	2	1400	3183	33	0.026(3)	3234	48	0.029(6)	3286	42	0.19(2)	3361	88	0.13(1)																
<b>B712A</b>	2	1600	3181	38	0.019(3)	3234	55	0.025(9)	3280	44	0.10(1)	3356	86	0.09(1)																
<b>B712C</b>	2	1600	3180	39	0.033(4)	3238	50	0.044(8)	3284	43	0.170(6)	3355	81	0.118(3)																
<b>B712D</b>	2	1600	<i>strong fluorescence</i>																											
<b>B712E</b>	2	1600	3180	39	0.048(2)	3234	59	0.102(3)	3284	45	0.231(4)	3343	103	0.32(1)																
<b>B712F</b>	2	1600	3181	33	0.028(2)	3247	75	0.151(5)	3286	38	0.170(3)	3345	103	0.279(3)																
<b>B727A</b>	2	1600	3182	46	0.046(1)	3238	55	0.056(2)	3284	43	0.20(2)	3354	100	0.17(1)																
<b>B727B</b>	2	1600	3179	41	0.043(7)	3237	67	0.066(2)	3284	42	0.21(2)	3351	110	0.17(4)																
<b>B727C</b>	2	1600	3180	44	0.030(3)	3235	50	0.036(3)	3282	44	0.13(1)	3359	94	0.114(9)																
<b>B727D</b>	2	1600	3181	44	0.028(7)	3235	75	0.08(2)	3285	42	0.18(2)	3355	96	0.19(5)																
<b>B727E</b>	2	1600	3181	39	0.038(3)	3242	71	0.117(7)	3285	44	0.21(1)	3345	99	0.29(1)																
<b>B727F</b>	2	1600	3181	41	0.035(2)	3243	70	0.11(1)	3286	39	0.277(9)	3340	103	0.28(2)																
<b>B714A</b>	3	1600	3179	44	0.03(1)	3235	49	0.04(2)	3282	44	0.12(4)	3349	108	0.13(5)																
<b>B714B</b>	3	1600	3183	46	0.058(1)	3237	56	0.088(2)	3288	49	0.322(3)	3356	83	0.250(2)																
<b>B714C</b>	3	1600	<i>strong fluorescence</i>																											
<b>B714D</b>	3	1600	3180	39	0.048(2)	3233	60	0.094(3)	3287	47	0.307(7)	3354	84	0.214(5)																

Numbers in parentheses reflect  $2\sigma$  standard errors in the significant digit from best-fit results.

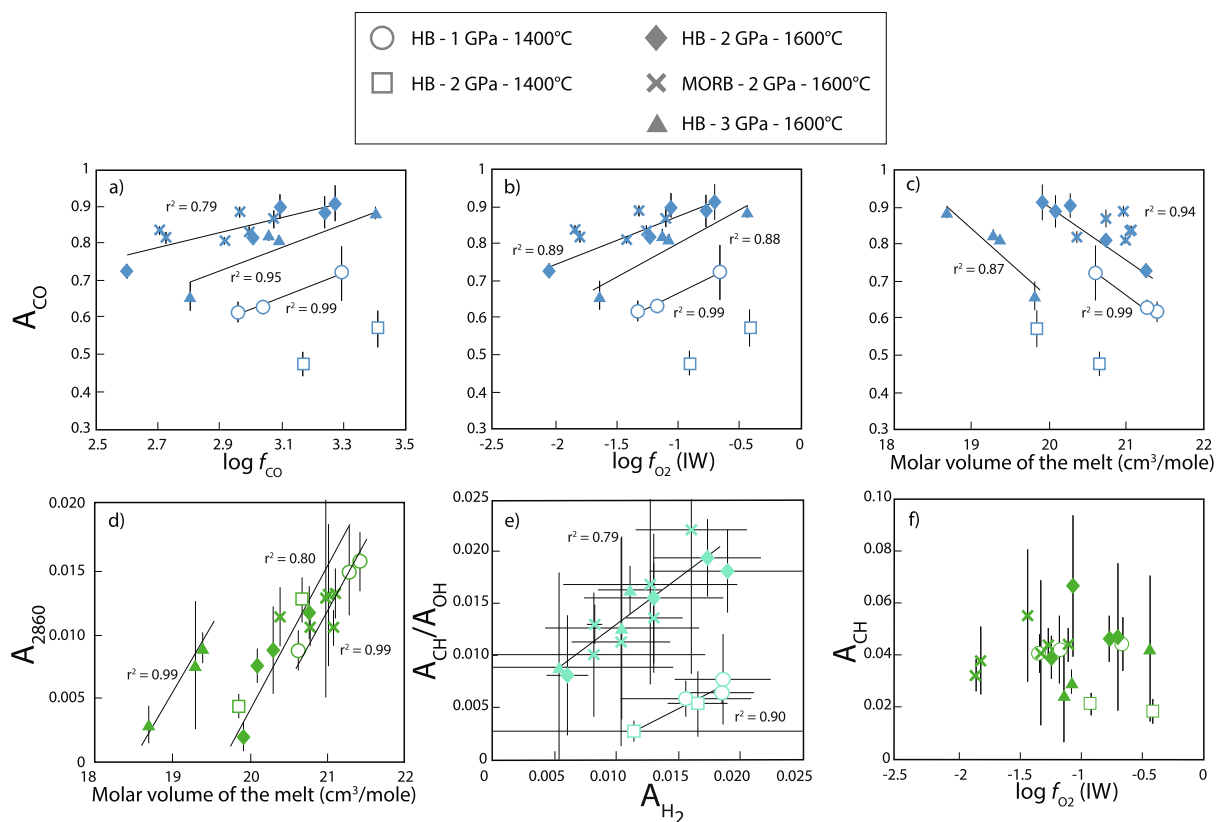
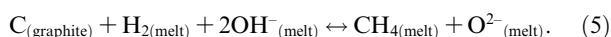


Fig. 6. Panels (a)–(c) show variation of the normalized band area near  $2120\text{ cm}^{-1}$  assigned to  $\text{C}\equiv\text{O}$  versus a)  $\log f_{\text{CO}}$ , (b)  $\log f_{\text{O}_2}$  relative to the IW buffer, and c) the molar volume of the melt. Panel (d) depicts variation of the peak area of the  $2860\text{ cm}^{-1}$  band with the molar volume of the melt. Panel (e) represents the variations of the sum of  $\text{CH}_4$  bands area (sum of  $2860\text{ cm}^{-1}$  and  $2900\text{ cm}^{-1}$  band areas) relative to that of the sum of OH bands area (sum of  $3500\text{ cm}^{-1}$  and  $3580\text{ cm}^{-1}$  band areas) with  $\text{H}_2$  band areas (sum of  $4130\text{ cm}^{-1}$  and  $4200\text{ cm}^{-1}$  band areas). Panel (f) shows the variations of the sum of  $\text{CH}_4$  bands area (sum of  $2860\text{ cm}^{-1}$  and  $2900\text{ cm}^{-1}$  band areas) with  $\log f_{\text{O}_2}$  relative to the IW buffer. On all panels, black lines are linear regressions.

Methane forms with as little as 400 ppm water in silicate glasses (Li et al., 2015b; Armstrong et al., 2015) and remains stable from moderately (IW-0.4) to very reduced conditions (IW-3; Ardia et al., 2013; Kadik et al., 2015, 2017). As Mysen and Yamashita (2010), Mysen et al. (2011) and Mysen (2015), we observed two peaks at  $2860$  and  $2900\text{ cm}^{-1}$  corresponding to C-H vibrations (Fig. 5a and b). The peak at  $2900\text{ cm}^{-1}$  is more intense and is assigned to C-H vibration in  $\text{CH}_4$  (Mysen et al., 2009 and references therein). Although Mysen and Yamashita (2010), Mysen et al. (2011) and Mysen (2015) assigned the peak around  $2870\text{ cm}^{-1}$  to C-H stretching in  $\text{Si-CH}_3$ , this complex is unlikely to be stable at high temperature (e.g., Renlund et al., 1991). In addition, the linear increase of the area of the peak  $2860\text{ cm}^{-1}$  with the increasing molar volume (Fig. 6d) suggests that this peak more likely corresponds to C-H stretching in  $\text{CH}_4$ . Consequently, the presence of two different peaks C-H stretching in  $\text{CH}_4$  more likely reflects multiple local environments in the silicate network, as it was observed for  $\text{N}_2$  and  $\text{H}_2$ .

We observe positive linear correlations between the peak areas of  $\text{CH}_4$  relative to that of OH ( $A_{\text{CH}}/A_{\text{OH}}$ ) and the peak area assigned to  $\text{H}_2$  (Fig. 6e). This suggests that, under reducing conditions,  $\text{CH}_4$  dissolves as:



The two distinct trends correspond to two different temperatures ( $1400$  and  $1600\text{ }^\circ\text{C}$ ), whereas no distinction is observed for different pressures. Ardia et al.'s (2013) model showed that  $\text{CH}_4$  solubility in reduced glasses increases with increasing H content and  $P$ , and decreasing  $f_{\text{O}_2}$ . In this study, we do not observe a clear relationship between the  $\text{CH}_4$  band area and  $f_{\text{O}_2}$  (Fig. 6f), likely because we cannot directly investigate the influence of  $f_{\text{O}_2}$  independently from H content.

Below IW, nitrogen is present as N-H,  $\text{N}\equiv\text{N}$  and  $\text{C}\equiv\text{N}$  species (Figs. 2 and 3). Kadik et al. (2017) detected NH species at  $f_{\text{O}_2}$  conditions down to IW-3.1 We observe a positive linear correlation between the sum of the  $3180$  and  $3285\text{ cm}^{-1}$  bands with the molar volume of the melt (Fig. 7a), whereas we note an absence of any relationship between the sum of the  $3235$  and  $3355\text{ cm}^{-1}$  bands and the molar volume (Fig. 7b). This implies that the  $3180$  and  $3285\text{ cm}^{-1}$  bands correspond to an N-H vibration of a neutral molecule, likely  $\text{NH}_3$ , and the  $3235$  and  $3355\text{ cm}^{-1}$  bands correspond to an NvH vibration of a bonded species, likely  $\text{NH}_2$  consistent with Mosenfelder et al. (2019). Based on a negative correlation between

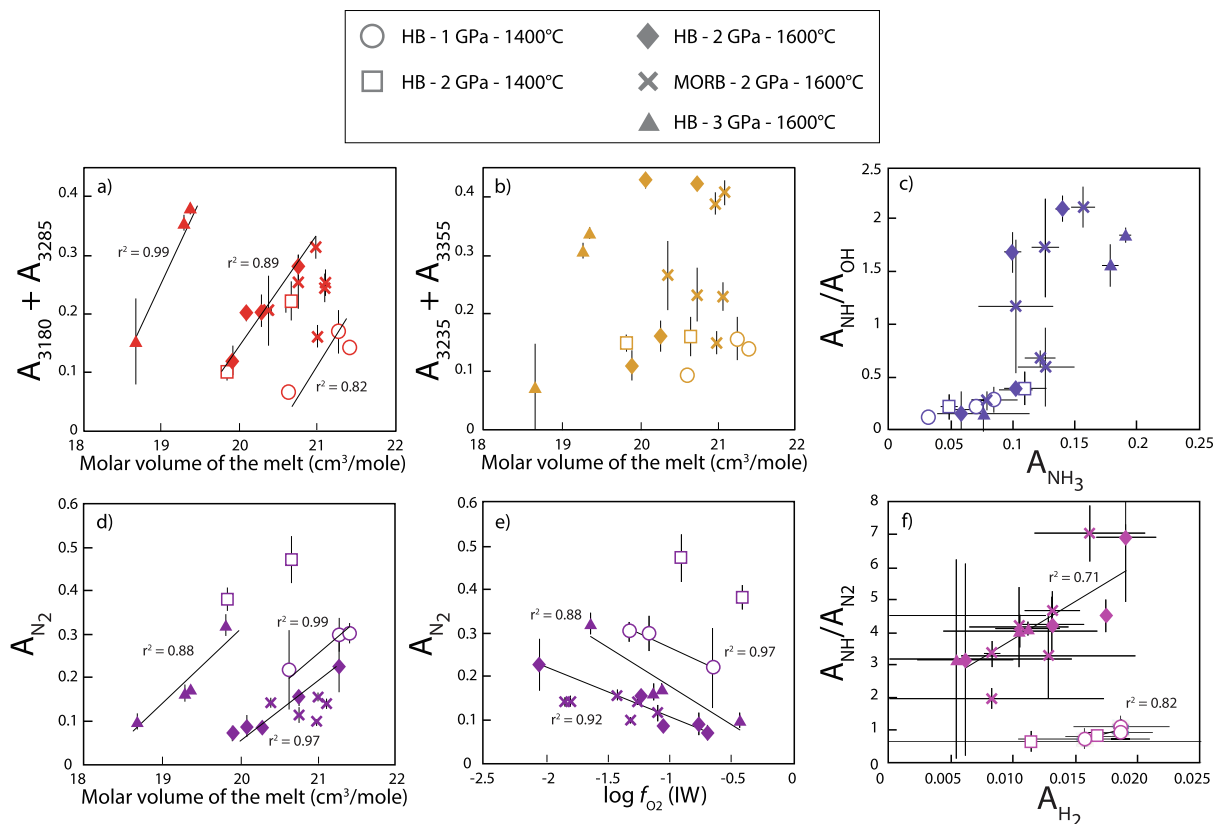


Fig. 7. Evolution of the sum of band areas of (a)  $3180\text{ cm}^{-1}$  and  $3285\text{ cm}^{-1}$  and (b)  $3235\text{ cm}^{-1}$  and  $3355\text{ cm}^{-1}$  bands with the calculated molar volumes of the melts. Panel (c) represents the variations of the sum of  $\text{NH}_2$  band areas (sum of  $3235\text{ cm}^{-1}$  and  $3355\text{ cm}^{-1}$  band areas) relative to that of the sum of OH band areas (sum of  $3500\text{ cm}^{-1}$  and  $3580\text{ cm}^{-1}$  band areas) with  $\text{NH}_3$  band areas (sum of  $3180\text{ cm}^{-1}$  and  $3285\text{ cm}^{-1}$  band areas). Panels (d) and (e) show the variation of the area of the sum of  $\text{N}_2$  band area (sum of band  $2330$  and  $2340\text{ cm}^{-1}$  areas) with (d) the molar volume of the melt, and (e)  $\log f_{\text{O}_2}$  relative to the IW buffer. Panel (f) shows the variations of the sum of NH band areas (sum of  $3180$ ,  $3235$ ,  $3285$  and  $3355\text{ cm}^{-1}$  band areas) relative to that of the sum of  $\text{N}_2$  band areas (sum of band  $2330$  and  $2340\text{ cm}^{-1}$  areas) with  $\text{H}_2$  band areas (sum of  $4130\text{ cm}^{-1}$  and  $4200\text{ cm}^{-1}$  band areas). On all panels, black lines are linear regressions.

$\text{NH}_2/\text{NH}_3$  ratio with decreasing melt polymerization, Mysen and Fogel suggested that  $\text{NH}_3$  interacts with bridging oxygen in the silicate melt to form Si-NH<sub>2</sub> and Si-OH bonds following:

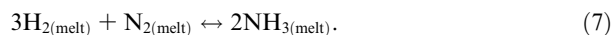


This equilibrium appears unaffected by  $P$  or  $T$  and is consistent with the observed positive trend between the peak areas of  $\text{NH}_2$  relative to that of OH ( $A_{\text{NH}_2}/A_{\text{OH}}$ ) and the peak area assigned to  $\text{NH}_3$  (Fig. 7c).

Dissolution of molecular  $\text{N}_2$  in silicate glasses has been inferred indirectly based on solubility studies (Libourel et al., 2003; Miyazaki et al., 2004), and observed previously by Raman spectroscopy (Roskosz et al., 2006; Mysen and Fogel, 2010; Mysen, 2013; Kadik et al., 2013; Li et al., 2015a). In reduced silicate glasses, N-H bonded species are generally considered to be the main dissolved species of nitrogen (Mysen et al., 2008; Mysen and Fogel, 2010; Kadik et al., 2013, 2015, 2017; Li et al., 2015a), and this providing a partial explanation for the reported enhanced nitrogen concentrations at reduced relative to oxidized conditions (Kadik et al. 2013, 2015; Li et al. 2016; Dalou et al. 2017). On the other hand, enhanced nitrogen

solubility at reduced conditions is also observed from 100 kPa gas mixing experiments, in which N-H species cannot play a role (Libourel et al. 2003). The use of a 458 nm excitation source improves the intensity of  $\text{N}_2$  scattering in N-rich samples, which allows the observation of variation of the  $\text{N}_2$  vibration intensity, and which cannot be attributed to air contamination (Fig. 3b). As for CO,  $\text{N}_2$  band area depends on molar volume of the melt,  $f_{\text{O}_2}$ ,  $P$  and  $T$  (Fig. 7d and e), but in contrast with CO band area,  $\text{N}_2$  peak area increases with the molar volume of the melt. Clearly, even as NH (or other nitride species) becomes important under reducing conditions (Libourel et al., 2003; Li et al., 2015a; Kadik et al., 2015, 2017; Mosenfelder et al., 2019),  $\text{N}_2$  band intensity remains non-negligible.

We observe positive linear correlations between the peak areas of NH complexes relative to that of  $\text{N}_2$  ( $A_{\text{NH}}/A_{\text{N}_2}$ ) and the peak area assigned to  $\text{H}_2$  (Fig. 7f). In addition, Mysen and Fogel (2010) observed increasing N solubility with increasing  $\text{H}_2$  fugacity: combined, these trends suggest the following equilibrium:



The two positive linear correlations between  $A_{\text{NH}}/A_{\text{N}_2}$  and  $A_{\text{H}_2}$  (Fig. 7f) correspond to the two different experimental temperatures, but do not depend on pressure. The  $A_{\text{NH}}/A_{\text{N}_2}$  ratio does not seem to increase with decreasing  $f_{\text{O}_2}$  or H/N ratio (Fig. S-4). This implies that the Equilibrium 7 depends mainly on temperature and  $\text{H}_2$  fugacity (Mysen and Fogel, 2010).

The observed  $\text{C}\equiv\text{N}$  vibration band at 2261–2268  $\text{cm}^{-1}$  is weak compared to  $\text{C}\equiv\text{O}$  vibration band (Fig. 3), even though the  $\text{C}\equiv\text{N}$  bond has a moderate Raman cross-section (Socrates, 2001). Compared to  $\text{C}\equiv\text{O}$  bonds,  $\text{C}\equiv\text{N}$  bonds (electronegativity of C: 2.55 versus N: 3.04) are less polarized, which may suggest either that  $\text{C}\equiv\text{N}$  complexes are in low abundance compared to other N species in these silicate glasses, or that the  $\text{C}\equiv\text{N}$  band intensity is weakened by the associated bonded metal ion (e.g.  $\text{X}-\text{C}\equiv\text{N}$ ; Colthrup et al. 1975, pp. 235–240). Nitrile groups coordinated to metal ions have  $\text{C}\equiv\text{N}$  stretching bands at higher wavenumber than that of  $\text{C}\equiv\text{N}$  bonded to O (2245–2256  $\text{cm}^{-1}$ ), C (2220–2240  $\text{cm}^{-1}$ ) or N (2210–2225  $\text{cm}^{-1}$ ) (Colthrup et al. 1975, pp. 235–240). Therefore, the features we observe at 2261–2268  $\text{cm}^{-1}$  are consistent with metal-cyanide complexes in the silicate network. The band area of  $\text{C}\equiv\text{N}$  stretching decreases significantly with increasing  $f_{\text{O}_2}$  (Fig. S-5). In addition, it decreases with increasing temperature and pressure (Fig. S-5). This may suggest that cyanide complex solubility in silicate melts increases under more reducing conditions and at lower  $P$ - $T$ , although caution should be taken to interpret Raman band areas in terms of solubility.

In anhydrous glasses quenched at 100 kPa, Libourel et al. (2003) observed a transition between the physical solubility (N dissolved as  $\text{N}_2$  in interstitial sites) and chemical solubility of N around IW. Below IW, N is assumed to dissolve as  $\text{N}^{3-}$ , i.e., nitride ions (Libourel et al., 2003). At conditions more reducing than IW-7, the solubility of N plateaus, presumably due to saturation in TiN (Libourel et al., 2003). The dominant vibrations for nitride stretching are near 405  $\text{cm}^{-1}$  for Ti-N (Dam et al., 2012) and near 800  $\text{cm}^{-1}$  for Si-N (Soignard and McMillan, 2004). Unfortunately, in the 300–900  $\text{cm}^{-1}$  range, the Raman signal is dominated by T-O-T and T-O bands (Fig. S-2), so it is difficult to ascertain the presence or absence of nitride species in our glasses.

Hirschmann et al. (2012) showed that  $\text{H}_2$  solubility depends on  $f_{\text{H}_2}$  and pressure and, based on comparison between basaltic and andesitic glass compositions, that the solubility is potentially consistent with a dissolution mechanism driven by the availability of free volumes in the melt. In agreement with this study, we observe a positive linear, although scattered, correlation between  $\text{H}_2$  peak area and the molar volume of the melt (Fig. S-5), whereas no correlation is observed with the  $f_{\text{O}_2}$  (Fig. S-5).

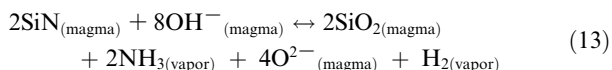
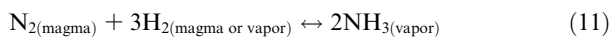
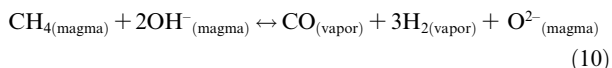
#### 4.2. Implications for the volatile speciation in early planetary mantles

Similar to previous studies (Mysen et al., 2008, 2009; Kadik et al., 2013, 2015, 2017; Wetzel et al., 2013; Chi et al., 2014; Armstrong et al., 2015; Yoshioka et al., 2015;

Li et al., 2015a; Mosenfelder et al., 2019), the Raman spectra presented here demonstrate that C-O-H-N speciation in reduced silicate glasses involves both chemically-bonded ionic complex and weakly interacting interstitial neutral molecules. Because the stability of individual species may be related to reactions with distinct dependencies on  $f_{\text{O}_2}$ ,  $f_{\text{H}_2\text{O}}$ , melt composition, temperature and pressure, the bulk solubilities of C and N in reduced glasses are complex. This explains in part why studies have found seemingly contradictory evidence for the importance of different species. For example, studies have shown that various proportions of C dissolved in reduced glasses are present as methane (Ardia et al., 2013; Wetzel et al., 2013; Chi et al., 2014; Kadik et al., 2014; Armstrong et al., 2015). C-H and N-H species solubilities may be particularly intricate, given the possibilities of both ionic and neutral complexes, the latter occupying interstitial sites in a manner similar to rare gases (Carroll and Stolper, 1993; Iacono-Marziano et al., 2010). Neutral substitution of  $\text{H}_2$  (Hirschmann et al. (2012),  $\text{N}_2$  (Libourel et al., 2003) and CO (Armstrong et al., 2015) are also relevant. However, more detailed comparison of their solubilities as a function of melt structure is needed. For noble gases, the influence of ionic porosity on the solubility is proportional to atomic radius (Carroll and Stolper, 1993). However, as the effective molecular radii of  $\text{H}_2$  and  $\text{N}_2$  are smaller than that of CO (74 and 110 pm versus 113 pm, respectively), they may be more effectively incorporated in available sites than CO.  $\text{NH}_3$  and  $\text{CH}_4$  have much larger effective radii (222 and 207 pm, respectively; Balmer, 2011, p. 733) and so, ionic species may be favored. This suggests that their solubilities are determined by more complex factors than variations in available interstitial sites.

From a broader perspective, the complex speciation of C and N complexes under reduced conditions is of considerable interest to degassing of reduced magma oceans. Although conventional treatments assume that atmospheres degassed from terrestrial magma oceans are oxidized (Matsui and Abe, 1986; Zahnle et al., 2007; Elkins-Tanton, 2008), reduced conditions may apply to magma oceans formed during accretion of the Earth, either in early stages when a solar nebular component predominated (Genda and Ikoma, 2008; Hirschmann et al., 2012; Sharp, 2017) or, potentially, during degassing of later magma oceans associated with the Moon-forming impact (Elkins-Tanton, 2012; Hirschmann, 2012; Schaefer and Fegley, 2017; Lammer et al., 2018; Lock et al., 2018). Reduced surface conditions are also expected above magma oceans from smaller planetary bodies (Zhang et al., 2017). Assuming a reduced magma ocean, magmatic volatiles species  $\text{H}_2$ ,  $\text{NH}_2$ ,  $\text{NH}_3$ ,  $\text{CH}_4$ , CO, CN,  $\text{N}_2$ , and OH can coexist and degas to species in resulting degassed atmospheres would be  $\text{H}_2$ ,  $\text{H}_2\text{O}$ , CO, and  $\text{NH}_3$ , with proportions depending on  $f_{\text{O}_2}$  (Schaefer and Fegley 2010). Consequently, release of those reduced magmatic species likely involved reactions such as:





A common view is of a Hadean atmosphere comprising  $\text{CO}_2$ ,  $\text{N}_2$ , and  $\text{H}_2\text{O}$ , with lesser amounts of  $\text{CO}$ ,  $\text{CH}_4$ , and  $\text{H}_2$  (Miyakawa et al. 2002, and references therein). However, a reduced magma ocean would have degassed an atmosphere bearing  $\text{H}_2$ ,  $\text{NH}_3$ ,  $\text{N}_2$ , and  $\text{CO}$ . Such reducing atmospheres are more favourable to biorganic synthesis than redox neutral atmospheres ( $\text{CO}_2$ - $\text{N}_2$ - $\text{H}_2\text{O}$ ; Dalai et al., 2016; Ferus et al., 2017).

The complex speciation of C-O-H-N volatiles in silicate liquids also is likely relevant to fractionation of H, C, and N isotopes during core formation and magma ocean degassing (e.g., Dalou et al., 2019). Such fractionation depends on the bonding environments of these elements, which are quite varied in the diverse possible neutral and ionic combinations. Thus, consideration of H, C, and N isotopic fractionation during planetary differentiation (Grady et al., 2004; Li et al., 2016; Wu et al., 2018; Dalou et al., 2019) should be conducted in tandem with characterization of relevant species bonding, including how these may be affected by intensive variables during magma ocean evolution and degassing.

## 5. CONCLUSIONS

Raman spectroscopy data on reduced volatile-bearing basaltic glasses show that the speciation of C-O-H-N species in basaltic melts is a complex function that varies with  $f_{\text{O}_2}$ ,  $\text{H}_2$  content, melt composition, temperature and pressure. Neutral species such as  $\text{H}_2$ ,  $\text{N}_2$ ,  $\text{CO}$ ,  $\text{NH}_3$  and  $\text{CH}_4$  are hosted in free volumes in the silicate network; however, the availability of free volumes is not the sole parameter that determines their solubility. Coexisting with these neutral molecules, other species such as  $\text{CN}^-$ ,  $\text{NH}_2^-$  and  $\text{OH}^-$  are chemically bonded. These differences between physical solubility (neutral molecules like  $\text{H}_2$ ,  $\text{N}_2$ ,  $\text{CO}$ ,  $\text{NH}_3$  and  $\text{CH}_4$  entering free volumes) and chemical solubility (ionic entities like  $\text{CN}^-$ ,  $\text{NH}_2^-$  and  $\text{OH}^-$  reacting with the melt network) influence the saturation pressure, temperature,  $f_{\text{O}_2}$  and  $f_{\text{H}_2}$  of those species in a magma ocean.

The coexistence  $\text{H}_2$ ,  $\text{NH}_2^-$ ,  $\text{NH}_3$ ,  $\text{CH}_4$ ,  $\text{CO}$ ,  $\text{CN}^-$ ,  $\text{N}_2$ , and  $\text{OH}^-$  dissolved in a reduced magma ocean implies diverse reactions during volatile species degassing to primitive planetary atmospheres and during their partitioning into core-forming metals. These reactions involve changes in C-O-H-N speciation, potentially influencing isotopic fractionations. Therefore, tracing the origin of volatile elements on Earth requires knowledge of their speciation during planetary formation processes.

## ACKNOWLEDGEMENTS

The authors thank Jed Mosenfelder and Anette von der Handt for helpful and inspiring discussions, and technical support. CD

thanks Giada Iacono-Marziano and Antonio Paonita for interesting discussions about ionic porosity calculations. CD and MH acknowledge support from the National Science Foundation grant AST1344133. SDJ acknowledges support from NSF EAR-1853521 and the David and Lucile Packard Foundation.

## APPENDIX A. SUPPLEMENTARY MATERIAL

Supplementary data to this article can be found online at <https://doi.org/10.1016/j.gca.2019.08.029>.

## REFERENCES

- Ardia P., Hirschmann M. M., Withers A. C. and Stanley B. D. (2013) Solubility of  $\text{CH}_4$  in a synthetic basaltic melt, with applications to atmosphere-magma ocean-core partitioning of volatiles and to the evolution of the Martian atmosphere. *Geochim. Cosmochim. Acta* **114**, 52–71.
- Armstrong L. S., Hirschmann M. M., Stanley B. D., Falksen E. G. and Jacobsen S. D. (2015) Speciation and solubility of reduced C-O-H-N volatiles in mafic melt: Implications for volcanism, atmospheric evolution, and deep volatile cycles in the terrestrial planets. *Geochim. Cosmochim. Acta* **171**, 283–302.
- Baert K., Meulebroeck W., Wouters H., Cosyns P., Nys K., Thienpont H. and Terryn H. (2011) Using Raman spectroscopy as a tool for the detection of iron in glass. *J. Raman Spectrosc.* **42**, 1789–1795.
- Balmer R. T. (2011) *Modern engineering thermodynamics-textbook with tables booklet*. Academic Press.
- Bourgue E. and Richet P. (2001) The effects of dissolved  $\text{CO}_2$  on the density and viscosity of silicate melts: a preliminary study. *Earth Planet. Sci. Lett.* **193**, 57–68.
- Cant N. W. and Little L. H. (1964) An Infrared Study of the Adsorption of Ammonia on Porous Vycor Glass. *Can. J. Chem.* **42**, 802–809.
- Carroll M. R. and Stolper E. M. (1993) Noble gas solubilities in silicate melts and glasses: New experimental results for argon and the relationship between solubility and ionic porosity. *Geochim. Cosmochim. Acta* **57**, 5039–5051.
- Chi H., Dasgupta R., Duncan M. S. and Shimizu N. (2014) Partitioning of carbon between Fe-rich alloy melt and silicate melt in a magma ocean—implications for the abundance and origin of volatiles in Earth, Mars, and the Moon. *Geochim. Cosmochim. Acta* **139**, 447–471.
- Colthrup N. B., Daly L. H. and Wiberly S. E. (1975) *Introduction to Infrared and Raman Spectroscopy*, 2nd Ed. Academic, New York.
- Dalai P., Kaddour H. and Sahai N. (2016) Incubating life: prebiotic sources of organics for the origin of life. *Elements* **12**, 401–406.
- Dalou C., Füre E., Deligny C., Piani L., Caumon M. C., Laumonier M., Boulliung J. and Edén M. (2019) Redox control on nitrogen isotope fractionation during planetary core formation. *Proc. Natl. Acad. Sci.* <https://doi.org/10.1073/pnas.1820719116>.
- Dalou C., Hirschmann M. M., Von Der Handt A., Mosenfelder J. and Armstrong L. S. (2017) Nitrogen and carbon fractionation during core-mantle differentiation at shallow depth. *Earth Planet. Sci. Lett.* **458**, 141–151.
- Dam D. T., Nam K. D., Song H., Wang X. and Lee J. M. (2012) Partially oxidized titanium carbonitride as a non-noble catalyst for oxygen reduction reactions. *Int. J. Hydrogen Energy* **37**, 15135–15139.

- Dasgupta R., Chi H., Shimizu N., Buono A. S. and Walker D. (2013) Carbon solution and partitioning between metallic and silicate melts in a shallow magma ocean: implications for the origin and distribution of terrestrial carbon. *Geochim. Cosmochim. Acta* **102**, 191–212.
- Dong J. L., Li X. H., Zhao L. J., Xiao H. S., Wang F., Guo X. and Zhang Y. H. (2007) Raman Observation of the Interactions between  $\text{NH}_4^+$ ,  $\text{SO}_4^{2-}$ , and  $\text{H}_2\text{O}$  in supersaturated  $(\text{NH}_4)_2\text{SO}_4$  Droplets. *J. Phys. Chem. B* **111**, 12170–12176.
- Dowty E. (1980) Crystal-chemical factors affecting the mobility of ions in minerals. *Am. Mineral.* **65**, 174–182.
- Elkins-Tanton L. T. (2008) Linked magma ocean solidification and atmospheric growth for Earth and Mars. *Earth Planet. Sci. Lett.* **271**, 181–191.
- Elkins-Tanton L. T. (2012) Magma oceans in the inner solar system. *Annu. Rev. Earth Planet. Sci.* **40**, 113–139.
- Ferus M., Pietrucci F., Saitta A. M., Knížek A., Kubelík P., Ivanek O. and Civiš S. (2017) Formation of nucleobases in a Miller-Urey reducing atmosphere. *Proc. Natl. Acad. Sci.* **114**, 4306–4311.
- Fortier S. M. and Giletti B. J. (1989) An empirical model for predicting diffusion coefficients in silicate minerals. *Science* **245**, 1481–1484.
- Foustoukos D. I. and Mysen B. O. (2012) D/H fractionation in the  $\text{H}_2$ – $\text{H}_2\text{O}$  system at supercritical water conditions: Compositional and hydrogen bonding effects. *Geochim. Cosmochim. Acta* **86**, 88–102.
- Frantz J. D., Dubessy J. and Mysen B. (1993) An optical cell for Raman spectroscopic studies of supercritical fluids and its application to the study of water to 500°C and 2000 bar. *Chem. Geol.* **106**, 9–26.
- Genda H. and Ikoma M. (2008) Origin of the ocean on the Earth: early evolution of water D/H in a hydrogen-rich atmosphere. *Icarus* **194**, 42–52.
- Grady M. M., Verchovsky A. B. and Wright I. P. (2004) Magmatic carbon in Martian meteorites: attempts to constrain the carbon cycle on Mars. *Int. J. Astrobiol.* **3**, 117–124.
- Hirschmann M. M. (2012) Magma ocean influence on early atmosphere mass and composition. *Earth Planet. Sci. Lett.* **341**, 48–57.
- Hirschmann M. M., Withers A. C., Ardia P. and Foley N. T. (2012) Solubility of molecular hydrogen in silicate melts and consequences for volatile evolution of terrestrial planets. *Earth Planet. Sci. Lett.* **345**, 38–48.
- Iacono-Marziano G., Paonita A., Rizzo A., Scaillet B. and Gaillard F. (2010) Noble gas solubilities in silicate melts: new experimental results and a comprehensive model of the effects of liquid composition, temperature and pressure. *Chem. Geol.* **279**, 145–157.
- Kadik A. A., Litvin Y. A., Koltashev V. V., Kryukova E. B., Plotnichenko V. G., Tsekhonya T. I. and Kononkova N. N. (2013) Solution behavior of reduced N–H–O volatiles in  $\text{FeO}$ – $\text{Na}_2\text{O}$ – $\text{SiO}_2$ – $\text{Al}_2\text{O}_3$  melt equilibrated with molten Fe alloy at high pressure and temperature. *Phys. Earth Planet. Inter.* **214**, 14–24.
- Kadik A. A., Koltashev V. V., Kryukova E. B., Plotnichenko V. G., Tsekhonya T. I. and Kononkova N. N. (2014) Solution behavior of C–O–H volatiles in  $\text{FeO}$ – $\text{Na}_2\text{O}$ – $\text{Al}_2\text{O}_3$ – $\text{SiO}_2$  melts in equilibrium with liquid iron alloy and graphite at 4 GPa and 1550°C. *Geochem. Int.* **52**, 707–725.
- Kadik A. A., Koltashev V. V., Kryukova E. B., Plotnichenko V. G., Tsekhonya T. I. and Kononkova N. N. (2015) Solubility of nitrogen, carbon, and hydrogen in  $\text{FeO}$ – $\text{Na}_2\text{O}$ – $\text{Al}_2\text{O}_3$ – $\text{SiO}_2$  melt and liquid iron alloy: influence of oxygen fugacity. *Geochem. Int.* **53**, 849–868.
- Kadik A. A., Koltashev V. V., Kryukova E. B., Tsekhonya T. I. and Plotnichenko V. G. (2017) Application of IR and Raman spectroscopy for the determination of the role of oxygen fugacity in the formation of N–C–O–H molecules and complexes in the iron-bearing silicate melts at high pressures. *Geochem. Int.* **54**, 1175–1186.
- Klimm K. and Botcharnikov R. E. (2010) The determination of sulfate and sulfide species in hydrous silicate glasses using Raman spectroscopy. *Am. Mineral.* **95**, 1574–1579.
- Lammer H., Zerkle A. L., Gebauer S., Tosi N., Noack L., Scherf M., Pilat-Lohinger E., Güdel M., Grenfell J. L., Godolt M. and Nikolaou A. (2018) Origin and evolution of the atmospheres of early Venus, Earth and Mars. *Astron. Astrophys. Rev.* **26**, 1–73.
- Lautié A., Froment F. and Novak A. (1976) Relationship between NH stretching frequencies and N...O distances of crystals containing NH...O hydrogen bonds. *Spectrosc. Lett.* **9**, 289–299.
- Le Losq C., Dalou C. and Mysen B. O. (2017) In situ study at high pressure and temperature of the environment of water in hydrous Na and Ca aluminosilicate melts and coexisting aqueous fluids. *J. Geophys. Res.* **122**, 4888–4899.
- Le Losq C., Mysen B. O. and Cody G. D. (2015) Water and magmas: insights about the water solution mechanisms in alkali silicate melts from infrared, Raman, and  $^{29}\text{Si}$  solid-state NMR spectroscopies. *Prog. Earth Planet. Sci.* **2**, 1–16.
- Li Y., Huang R., Wiedenbeck M. and Keppler H. (2015a) Nitrogen distribution between aqueous fluids and silicate melts. *Earth Planet. Sci. Lett.* **411**, 218–228.
- Li Y., Dasgupta R. and Tsuno K. (2015b) The effects of sulfur, silicon, water, and oxygen fugacity on carbon solubility and partitioning in Fe-rich alloy and silicate melt systems at 3 GPa and 1600°C: Implications for core–mantle differentiation and degassing of magma oceans and reduced planetary mantles. *Earth Planet. Sci. Lett.* **415**, 54–66.
- Li Y. F., Marty B., Shekela S., Zimmermann L. and Keppler H. (2016) Nitrogen isotope fractionation during terrestrial core–mantle separation. *Geochem. Perspect.* **2**, 138–147.
- Li Y., Dasgupta R. and Tsuno K. (2017) Carbon contents in reduced basalts at graphite saturation: Implications for the degassing of Mars, Mercury, and the Moon. *J. Geophys. Res. Planets* **122**, 1300–1320.
- Libourel G., Marty B. and Humbert F. (2003) Nitrogen solubility in basaltic melt. Part I. Effect of oxygen fugacity. *Geochim. Cosmochim. Acta* **67**, 4123–4135.
- Lin-Vien D., Colthup N. B., Fateley W. G. and Grasselli J. G. (1991) *The handbook of infrared and Raman characteristic frequencies of organic molecules*. Elsevier.
- Lock S. J., Stewart S. T., Petaev M. I., Leinhardt Z., Mace M. T., Jacobsen S. B. and Cuk M. (2018) The origin of the Moon within a terrestrial synestia. *J. Geophys. Res. Planets* **123**, 910–951.
- Lofthus A. and Krupenie P. H. (1977) The spectrum of molecular nitrogen. *J. Phys. Chem. Ref. Data* **6**, 113–307.
- Long D. A. (1977) *Raman spectroscopy*, McGraw. Hill Higher Education.
- Marrocchi Y. and Toplis M. J. (2005) Experimental determination of argon solubility in silicate melts: An assessment of the effects of liquid composition and temperature. *Geochim. Cosmochim. Acta* **69**, 5765–5776.
- Matsui T. and Abe Y. (1986) Evolution of an impact-induced atmosphere and magma ocean on the accreting Earth. *Nature* **319**, 303–305.
- McMillan P. F. and Remmele R. L. (1986) Hydroxyl sites in  $\text{SiO}_2$  glass; a note on infrared and Raman spectra. *Am. Mineral.* **71**, 772–778.

- Médard E., McCammon C. A., Barr J. A. and Grove T. L. (2008) Oxygen fugacity, temperature reproducibility, and H<sub>2</sub>O contents of nominally anhydrous piston-cylinder experiments using graphite capsules. *Am. Mineral.* **93**, 1838–1844.
- Miyazaki A., Hiyagon H., Sugiura N., Hirose K. and Takahashi E. (2004) Solubilities of nitrogen and noble gases in silicate melts under various oxygen fugacities: implications for the origin and degassing history of nitrogen and noble gases in the Earth. *Geochim. Cosmochim. Acta* **68**, 387–401.
- Mosenfelder J. L., Von Der Handt A., Füre E., Dalou C., Hervig R. L., Rossman G. R. and Hirschmann M. M. (2019) Nitrogen incorporation in silicates and metals: results from SIMS, EPMA, FTIR, and laser-extraction mass spectrometry. *Am. Mineral.* **104**, 31–46.
- Muthuselvi C., Pandiarajan S., Athimoolam S., Krishnakumar R. V. and Manikandan A. (2017) Structural and Optical Properties of NLO Material: 4-Sulfamoylanilinium Dihydrogen Phosphate. *Adv. Sci. Eng. Med.* **9**, 931–942.
- Mysen B. (2016) Experimentally-determined carbon isotope fractionation in and between methane-bearing melt and fluid to upper mantle temperatures and pressures. *Earth Planet. Sci. Lett.* **445**, 28–35.
- Mysen B. (2018) Solution mechanisms of COHN fluids in melts to upper mantle temperature, pressure, and redox conditions. *Am. Mineral.* **103**, 1780–1788.
- Mysen B. O. (2013) Structure–property relationships of COHN-saturated silicate melt coexisting with COHN fluid: A review of in-situ, high-temperature, high-pressure experiments. *Chem. Geol.* **346**, 113–124.
- Mysen B. O. (2015) Carbon speciation in silicate-COH melt and fluid as a function of redox conditions: An experimental study, in situ to 1.7 GPa and 900°C. *Chem. Geol.* **100**, 872–882.
- Mysen B. O. and Fogel M. L. (2010) Nitrogen and hydrogen isotope compositions and solubility in silicate melts in equilibrium with reduced (N+H)-bearing fluids at high pressure and temperature: Effects of melt structure. *Am. Mineral.* **95**, 987–999.
- Mysen B. O. and Yamashita S. (2010) Speciation of reduced C–O–H volatiles in coexisting fluids and silicate melts determined in-situ to ~1.4 GPa and 800°C. *Geochim. Cosmochim. Acta* **74**, 4577–4588.
- Mysen B. O., Yamashita S. and Chertkova N. (2008) Solubility and solution mechanisms of N–O–H volatiles in silicate melts at high pressure and temperature-amine groups and hydrogen fugacity. *Am. Mineral.* **93**, 1760–1770.
- Mysen B. O., Fogel M. L., Morrill P. L. and Cody G. D. (2009) Solution behavior of reduced C–O–H volatiles in silicate melts at high pressure and temperature. *Geochim. Cosmochim. Acta* **73**, 1696–1710.
- Mysen B. O., Kumamoto K., Cody G. D. and Fogel M. L. (2011) Solubility and solution mechanisms of C–O–H volatiles in silicate melt with variable redox conditions and melt composition at upper mantle temperatures and pressures. *Geochim. Cosmochim. Acta* **75**, 6183–6199.
- Nakamoto K. (2009) *Infrared and Raman spectra of inorganic and coordination compounds, Part A: Theory and applications in inorganic chemistry*, 419p. John Wiley and Sons, Hoboken, New Jersey.
- Nowak M. and Behrens H. (1995) The speciation of water in haplogranitic glasses and melts determined by in situ near-infrared spectroscopy. *Geochimica et Cosmochimica Acta* **59** (16), 3445–3450.
- Nowak M., Porbatzki D., Spickenbom K. and Diedrich O. (2003) Carbon dioxide speciation in silicate melts: a restart. *Earth Planet. Sci. Lett.* **207**, 131–139.
- Paonita A. (2005) Noble gas solubility in silicate melts: a review of experimentation and theory, and implications regarding magma degassing processes. *Ann. Geophys.* **48**, 648–669.
- Parker G. K. and Hope G. A. (2010) A Spectroelectrochemical Investigation of the Interaction of Gold with Cyano-Containing Ligands. *ECS Trans.* **28**, 223–235.
- Renlund G. M., Prochazka S. and Doremus R. H. (1991) Silicon oxycarbide glasses: Part I. *Preparation and chemistry*. *J. Mater. Res.* **6**, 2716–2722.
- Richter T. M., Alt N. S., Schlücker E. and Niewa R. (2015) Ammonothermal Synthesis and Characterization of Li<sub>4</sub>Zn(NH<sub>2</sub>)<sub>4</sub>(NH<sub>2</sub>)<sub>2</sub>. *Z. Anorg. Allg. Chem.* **641**, 1016–1023.
- Roskosz M., Mysen B. O. and Cody G. D. (2006) Dual speciation of nitrogen in silicate melts at high pressure and temperature: an experimental study. *Geochim. Cosmochim. Acta* **70**, 2902–2918.
- Rubie D. C., Frost D. J., Mann U., Asahara Y., Nimmo F., Tsuno K., Kegler P., Holzheid A. and Palme H. (2011) Heterogeneous accretion, composition and core–mantle differentiation of the Earth. *Earth Planet. Sci. Lett.* **301**, 31–42.
- Schaefer L. and Fegley, Jr, B. (2017) Redox States of Initial Atmospheres Outgassed on Rocky Planets and Planetesimals. *Astrophys. J.* **843**, 1–18.
- Schmidt B. C., Holtz F. M. and Beny J.-M. (1998) Incorporation of H<sub>2</sub> in vitreous silica, qualitative and quantitative determination from Raman and infrared spectroscopy. *J. Non-Cryst. Solids* **240**, 91–103.
- Sharp Z. D. (2017) Nebular ingassing as a source of volatiles to the terrestrial planets. *Chem. Geol.* **448**, 137–150.
- Siebert J., Badro J., Antonangeli D. and Ryerson F. J. (2013) Terrestrial accretion under oxidizing conditions. *Science* **339**, 1194–1197.
- Stanley B. D., Hirschmann M. M. and Withers A. C. (2014) Solubility of COH volatiles in graphite-saturated martian basalts. *Geochim. Cosmochim. Acta* **129**, 54–76.
- Socrates G. (2001). *Infrared and Raman Characteristic Group Frequencies—Tables and Charts* **347**, p.,
- Soignard E. and McMillan P. F. (2004) Raman spectroscopy of  $\gamma$ -Si<sub>3</sub>N<sub>4</sub> and  $\gamma$ -Ge<sub>3</sub>N<sub>4</sub> nitride spinel phases formed at high pressure and high temperature: Evidence for defect formation in nitride spinels. *Chem. Mater.* **16**, 3533–3542.
- Sowerby J. R. and Keppler H. (1999) Water speciation in rhyolitic melt determined by in-situ infrared spectroscopy. *Ame. Mineral.* **84**, 1843–1849.
- Thomas S. M., Jacobsen S. D., Bina C. R., Reichart P., Moser M., Hauri E. H., Koch-Müller M., Smyth J. R. and Dollinger G. (2015) Quantification of water in hydrous ringwoodite. *Front. Earth Sci.* **2**, 1–19.
- Tucker J. M. and Mukhopadhyay S. (2014) Evidence for multiple magma ocean outgassing and atmospheric loss episodes from mantle noble gases. *Earth Planet. Sci. Lett.* **393**, 254–265.
- Turnbull D. and Cohen M. H. (1961) Free-volume model of the amorphous phase: glass transition. *J. Chem. Phys.* **34**, 120–125.
- Watenphul A., Wunder B. and Heinrich W. (2009) High-pressure ammonium-bearing silicates: Implications for nitrogen and hydrogen storage in the Earth’s mantle. *Am. Mineral.* **94**, 283–292.
- Wetzel D. T., Rutherford M. J., Jacobsen S. D., Hauri E. H. and Saal A. E. (2013) Degassing of reduced carbon from planetary basalts. *Proc. Natl. Acad. Sci.* **110**, 8010–8013.
- Wu J., Desch S. J., Schaefer L., Elkins-Tanton L. T., Pahlevan K. and Buseck P. R. (2018) Origin of Earth’s water: chondritic inheritance plus nebular ingassing and storage of hydrogen in the core. *J. Geophys. Res. Planets* **123**, 2691–2712.

Yoshioka T., Mccammon C., Shehka S. and Keppler H. (2015) The speciation of carbon monoxide in silicate melts and glasses. *Am. Mineral.* **100**, 1641–1644.

Zahnle K., Arndt N., Cockell C., Halliday A., Nisbet E., Selsis F. and Sleep N. H. (2007) Emergence of a habitable planet. *Space Sci. Rev.* **129**, 35–78.

Zhang H. L., Hirschmann M. M., Cottrell E. and Withers A. C. (2017) Effect of pressure on  $\text{Fe}^{3+}/\Sigma\text{Fe}$  ratio in a mafic magma and consequences for magma ocean redox gradients. *Geochim. Cosmochim. Acta* **204**, 83–103.

*Associate editor:* Christopher Herd